

A novel electric drive description to bridge the gap between energetic and equivalent-circuit models

Original

A novel electric drive description to bridge the gap between energetic and equivalent-circuit models / Grano, E., De Carvalho Pinheiro, H., Carello, M.. - In: PROCEEDINGS OF THE INSTITUTION OF MECHANICAL ENGINEERS. PART D, JOURNAL OF AUTOMOBILE ENGINEERING. - ISSN 0954-4070. - ELETTRONICO. - 40:4(2026), pp. 1937-1957. [10.1177/09544070251330340]

Availability:

This version is available at: 11583/3000070 since: 2025-05-12T15:30:44Z

Publisher:

SAGE

Published

DOI:10.1177/09544070251330340

Terms of use:

This article is made available under terms and conditions as specified in the corresponding bibliographic description in the repository

Publisher copyright

(Article begins on next page)

A Novel Electric Drive Description to Bridge the Gap between Energetic and Equivalent-Circuit Models

Elia Grano*, Henrique de Carvalho Pinheiro, Massimiliana Carello

Department of Mechanical and Aerospace Engineering, Politecnico di Torino, corso Duca degli Abruzzi 24, Torino 10129, Italy

Abstract

This paper introduces a novel approach to electric drive modeling, addressing the limitations of methods commonly applied for electric vehicle simulations. Energetic approaches, commonly used for powertrain control, offer computational efficiency but lack the granularity required to model motor currents and voltages accurately. Moreover, their reliance on fixed voltage levels renders them unreliable when supply voltages vary. On the other end of the spectrum, equivalent-circuit models provide detailed descriptions but entail high complexity and computational burden due to the explicit implementation of low-level motor control and extensive input data requirements. The proposed approach bridges this gap by integrating an equivalent circuit electric motor description and a phenomenological inverter model. By leveraging on lookup tables for stator currents references generation, the proposed methodology enables accurate representation of motor currents and voltages without the need for explicit implementation of the low-level motor control. Furthermore, a multi-step torque reference saturation process guarantees compliance of motor operation with the limitations imposed by the energy storage system. This streamlined process ensures computational efficiency while capturing essential aspects of the electric drive behavior. By combining elements of both energetic and equivalent-circuit modeling, the presented approach achieves a favorable balance between computational efficiency and modeling accuracy, making it well-suited for EVs simulations. Validation against experimental data from a Tesla Model 3 Long-Range AWD demonstrates the efficacy of the generalized model. Practical implementation examples further underscore the applicability and utility of the proposed methodology.

Keywords: sustainable mobility; electric vehicles; hybrid vehicles; electric drive; inverter; electric motor; electric drive control.

1. Introduction

Electric Vehicles (EVs) are not a novelty of the 21st century. Indeed, the early automotive industry was way more heterogeneous in terms of powertrain architecture than today, with approximately 40% of the vehicles on the roads that were steam-powered in the early 1900s, 22% gasoline-powered and 38% battery-powered [1]. Unlike other vehicle architectures at that time, electric cars were quiet, required little effort to start and did not suffer from fumes or vibrations, factors that greatly contributed to EVs diffusion. Anyway, after a short period of market success, the limited range and top speed of EVs, as well as the long recharge time, caused a reduction in their market share, resulting in their practically complete substitution by the vehicles from Benz and Ford [2], which were powered by Internal Combustion Engines (ICEs).

Interest in the EV technology started coming back in the 1990s, pushed by the first version of the Zero-Emission Vehicles mandate being announced in California [3]. In the same years, the European Commission started enforcing legislations to limit vehicle emissions [4]. Legislations evolved over the years, and the European emission standards are today the most important initiatives worldwide for the control of tailpipe criteria pollutants from vehicles, and they are expected to be further harshened by 2025 with the introduction of the Euro 7 emission standards [5]. Besides,

* E-mail address: elia.grano@polito.it

<http://dx.doi.org/???>

1077-3142/© 2017 Elsevier Inc. All rights reserved.

severe limitations on tailpipe GreenHouse Gases (GHGs) emissions are expected in the European market, with the programs like “Fit for 55” [6] that have already been approved and the possibility to mandate zero tailpipe GHGs emissions by 2035 [7].

The favourable legislation push that started in the ‘90s made impossible for big carmakers to ignore the EV technology. The revived research interested resulted in fast advancements of key technologies (and still does today) like lithium-ion batteries, which saw both great performance improvements [8, 9] and price reduction [10]. Today the future of electric vehicles market looks bright, with an estimated compound annual growth rate growth of about 20% in the Chinese, European and US markets [11, 12].

Important challenges still exist for EVs, with safety [13, 14], range [15] and recharging times [16] being perceived as major roadblocks by most customers. Besides, limitations of the electric grid [17, 18], energy consumption for manufacturing [19], raw materials supply [20] and batteries recycling [21, 22, 23] are today open points for automakers and legislators. Such important challenges rise the question whether automotive will be the future of mobility or not [24], and evidence exist that automobile might probably lose some of its dominance but will remain the most flexible mode of transport.

After more than thirty years of continuous development, EVs’ technology still evolves fast today. Besides improvements in vehicle mass, aerodynamics, performance [25] and comfort, electrochemical sources continue to promise evolution [26, 27, 28, 29]. Lithium air [30], lithium-sulphur [31, 32], sodium superoxide [33, 34] and solid-state [35, 36, 37] are promising battery technologies and chemistries that will likely be ready for mass production in the next years. Research effort is also dedicated to the investigation of alternative energy vectors like hydrogen [38, 39], to the reduction of non-combustion particulate emissions [40] and to the improvement of electric drives hardware and control [41, 42, 43, 44, 45].

Modern Life Cycle Assessment (LCA) methodologies evidence that, even with a power mix dominated by fossil fuels, EVs can reduce noxious emissions with respect to conventional vehicles [46]. Cutting-edge technologies like Advanced Driver Assistance Systems (ADASs) and vehicle connectivity may help at further reducing vehicle’s carbon footprint. Indeed, the increased amount of information that can be accessed by vehicles equipped with technologies like these can be effectively exploited to optimize propulsion system control with respect to conventional ones [47, 48, 49]. Vehicle connectivity can also contrast range anxiety keeping into account the availability of charging stations and the battery state during path planning [50, 51, 52, 53, 54], potentially increasing EVs acceptance to customers.

Because of all these facts and many others that have not been mentioned, the design of modern road vehicles is a complex task that spans through multiple domains of engineering. In the attempt to facilitate it, a standardized procedure for EVs powertrain sizing has been developed, the “PerFECT Design Tool” [55], whose name is the acronym of “performance”, “energy”, “currents” and “temperature”. The name comes from the fact that this vehicle design procedure decomposes the EVs’ powertrain sizing process into sequential steps, each of which focuses on a specific aspect. The “performance” level is based on a simple vehicle model to define the motor torque and power needed to meet the target performance. Similarly, the “energy” level uses an energetic vehicle model to determine the ESS energy and power requirements. The “currents” level implements an electromechanical description of the vehicle to investigate the interactions between the electric drive(s) and the ESS(s). Finally, the “temperature” level aims at understanding which are the vehicle cooling requirements.

This paper describes the electric-drive model that has been implemented at the “currents” level of the PerFECT Design Tool, which allows to investigate the performance of EVs’ powertrain without neglecting the interdependent and complex relations that regulate the behaviour of its subsystems. Indeed, the biggest challenge in the implementation of the “currents” level was the development of an electric drive model capable of providing information about stator currents and voltages while being general enough to represent a multitude of different motor technologies. Additionally, the electric drive model was developed with the goal of keeping the amount of input data as low as possible, in order to facilitate its use at the early stages of the vehicle design process, and it had to be a good trade-off between accuracy and computational complexity, delivering reliable results while being adequate for the purpose of EVs simulations over long driving missions. The combination of two innovative modelling approaches allowed to meet all these requirements: a standardized motor control strategy based on the use of LookUp Tables (LUTs) and a phenomenological inverter model.

The motor control strategy leverages on the use of two LUTs to provide d - and q -axis stator current references. The LUTs are obtained by means of a numerical optimization algorithm that calculates the stator currents pair that

better satisfy the selected optimality criterion under each possible motor operating condition [56]. This approach has the advantage of being simple, flexible, applicable to both synchronous and induction machines and capable of running the motor over a wide range of supply voltages thanks to a standardized flux weakening policy. The LUTs generation algorithm is compatible with simple equivalent circuit motor models that require little input data to run, but it can be easily customized to work on more accurate motor models, giving the chance to customize the level of detail based on the amount of information available about the electric machine [57].

The phenomenological [58] inverter model was developed with the aim of accurately describing the interactions between the electric drive and the ESS(s) without an explicit implementation of the low-level motor control, which would entail modelling complexity and a large computational burden for EVs simulations [59]. Additionally, the model is supposed to be flexible enough to be used for different EV architectures without significant modifications from the user, representing a plug-and-play component in the PerfECT Design Tool’s library. The result is a model capable of accounting for the main effects of the inverter operation on vehicle performance, including the propagation to the electric motor of power and voltage limitations imposed by the ESS and the implementation of the motor control policy. Overall, the phenomenological inverter model does not intend to replicate the physical operation of inverter’s hardware but only its role as a motor controller affected by the availability of power and voltage from the ESS.

Two different variants of the electric drive model are presented in this work. The first is a high-fidelity version applicable to single-motor single-ESS EVs only. The other is a generalized version that is suitable for multiple-motor and/or multiple-ESS EV architectures. Additionally, a standardized flux weakening policy is presented. The generalized model is validated by comparing simulation results with measurements collected on an experimental campaign using the 2021 Long-Range AWD version of the Tesla Model 3, and an example of practical implementation of the proposed methodology to model a single-motor single-ESS vehicle is proposed and discussed.

2. Electric drive model

In the context of system-level EVs simulations, it is a very common practice to model electric drives by means of energetic approaches, especially in the field of powertrain control. In most cases the electric drive is modelled by means of efficiency maps that include the effect of both motor and inverter power losses [60, 61], but some literature references exist that propose analytical expressions for power losses estimation [62]. Energetic approaches have the great advantage of being simple and computationally inexpensive, being suitable for real-time powertrain control [61, 63, 64], but they cannot model stator current and voltage components effectively. Indeed, even though they can be used to estimate currents and voltages at the DC side of the inverter [65], they cannot provide any information about stator current and voltage components. Another drawback is that efficiency maps are generally obtained at a fixed voltage level and must therefore be considered unreliable in case the supply voltage is modified. Because of these reasons, a purely energetic approach is not sufficiently detailed for the purpose of the PerfECT Design Tool’s “currents” level.

Many authors have proposed EV models that implement accurate equivalent-circuit descriptions of the electric drive [66, 67]. While being capable of describing the trend of the electrical quantities in the electric drive, including those that are of interest to the PerfECT Design Tool’s “currents” level, their complexity is very high. These models are difficult to build and run, requiring an explicit implementation of the low-level motor control, and need a large amount of input data. Because of such a high level of detail, they represent a significant computational burden slowing down the simulation. The use of average-value inverter models might help at reducing complexity [68], but the result would still be unnecessarily detailed for the purpose.

The proposed approach to electric drive modelling aims at bridging the gap between energetic and equivalent circuit electric drive models, obtaining information about currents and voltages in the motor without having an explicit implementation of the low-level motor control. An equivalent circuit model description in the d - q reference frame is used for the electric motor, which takes as inputs the stator voltages from the inverter model. The low-level motor control is embedded into two LUTs, which associate a stator current components pair to an input torque reference signal. A three-step process of saturation of the torque reference is implemented to respect the limitations imposed by the ESS on motor operation.

2.1. Inverter model

From the physical point of view, a very simple model is used for the inverter, modelling it as a black box characterized by an efficiency value, η_{inv} . Depending on the desired level of detail, the value of inverter efficiency may either be constant or change depending on the working condition.

$$P_{AC} = \begin{cases} \eta_{inv} P_{DC} & \text{if } P_{DC} \geq 0 \\ \frac{1}{\eta_{inv}} P_{DC} & \text{if } P_{DC} < 0 \end{cases} \quad (1)$$

where P_{AC} is the power at the AC side of the inverter and P_{DC} is the power at its DC side, with power that is defined as positive when the inverter is transferring it from the ESS to the electric motor.

To prevent the inverter from operating in its non-linear modulation region, a limitation to the AC voltage amplitude based on the available DC voltage is imposed, as described by Equation 2.

$$V_{AC} \leq k_{mod} v_{DC} \quad (2)$$

where k_{mod} is a constant that depends on the applied modulation technique [69].

The AC voltage, v_{AC} , depends on the operating condition of the electric motor [70, 71, 72] while the DC voltage, v_{DC} , depends on the ESS current output [73, 74, 75]. Therefore, the AC voltage limitation has important effects on the electric motor operation as it imposes the maximum stator voltage at which the motor can operate. In addition to the power loss and to the AC voltage limitation, the inverter must also propagate the ESS power limitations to the electric motor, meaning that the combination of d - and q - axis stator current outputted by the inverter must be compatible with ESS operation. This process is explained in Section 4 for the case of the single-motor, single-ESS model, and in Section 5 for the multiple-motor, multiple-ESS model.

As anticipated in the introduction, the inverter is the powertrain component that actuates the motor control logic, which is implemented in the model by means of the bidimensional LUTs presented in [56] to avoid having an explicit implementation of the low-lever motor control. Depending on the desired level of detail, the dimensionality of the LUTs may be increased, as demonstrated in [57]. Further details about the LUTs and their input signals are available in Section 3.

2.2. Electric motor model

The electric motor is modelled with an equivalent circuit approach in the d - q reference frame. Depending on the amount of data available and the required level of accuracy, different equivalent circuit models can be used. The simplest approach is the one presented in [56], in which a simple formulation for both synchronous and induction motors is discussed. This approach is the one adopted in Section 7.2, in which the synchronous motor equivalent circuit model equations and their implementation in MATLAB/Simulink are presented.

A more detailed approach is presented in [57], in which the procedure for the calculation of three-dimensional LUTs for the control of an induction machine is disserted, based on the use of a detailed motor equivalent circuit model featuring linear iron loss resistance model from [76], nonlinear magnetizing inductance model from [77] and mechanical loss model from [78, 79].

3. LUT-based stator current references generation

The electric motor control strategy is based on LUTs for d - and q -axis stator current reference generation requiring commanded torque, T^* , and the stator flux limit, $\lambda_{s,lim}$, as inputs. The LUTs are generated by means of the algorithm presented in [56], which discretizes the operating domain of the electric motor and solves a numerical optimization problem for each possible motor operating condition. The solution of the optimization problem represents the best combination of d - and q -axis stator currents for the specific operating conditions considered.

In the case of bi-dimensional LUTs, the discretization of the motor operating domain into sample points is made by means of two vectors, each spanning through a different dimension:

- Electromagnetic torque samples vector, T^V , obtained by subdividing the motor torque range $[T_{min}, T_{max}]$ into evenly spaced samples, with T_{min} and T_{max} corresponding respectively to the minimum and maximum transient torque that the machine can produce.
- Stator flux limit samples vector, λ_s^V , obtained by subdividing the stator flux range $[0, \lambda_{s,max}]$ into evenly spaced samples, with $\lambda_{s,max}$ corresponding to the maximum stator flux that the machine can be operated at.

Further information about the process of discretization of the motor operating domain and LUTs generation can be found in [56, 57].

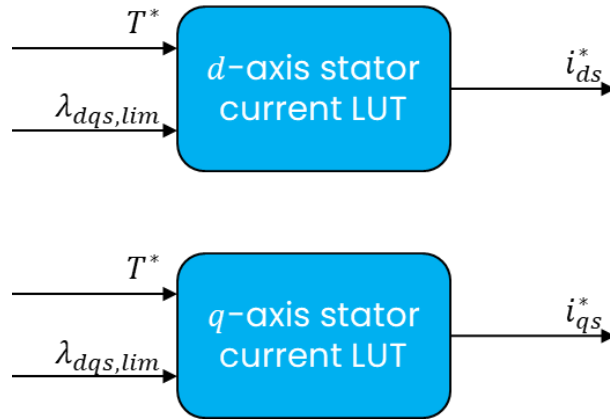


Fig. 1. Inputs and outputs of the LUTs for stator current references generation.

3.1. Generation of the torque reference signal

One of the commonest approaches to generate the torque reference signal is to use a longitudinal speed-tracking PI controller, like [80], in combination with a policy to convert the acceleration and deceleration commands into a torque reference signal. An example is shown in Figure 2.

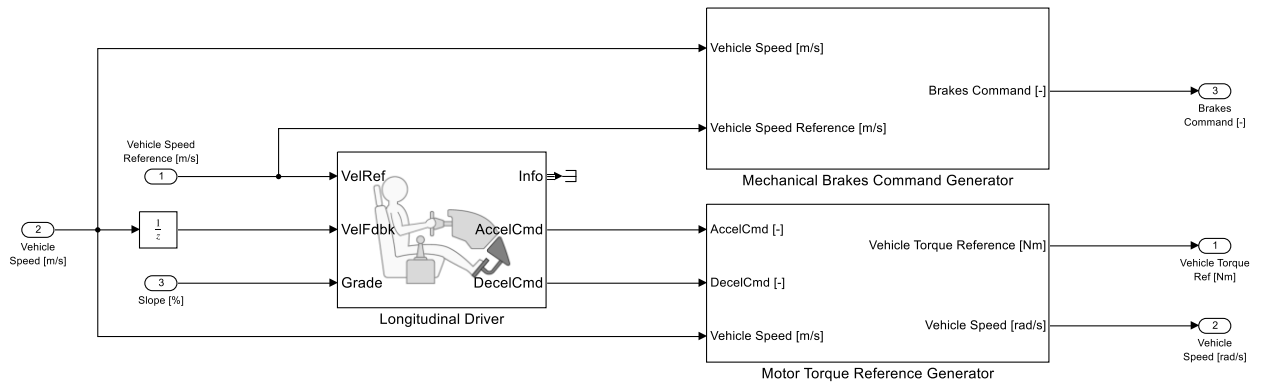


Fig. 2. Schematics of a simple motor torque reference generator.

Figure 3 proposes a practical example of how the “Motor Torque Reference Generator” block from Figure 2 can be implemented, converting driver pedal commands into a motor torque reference signal.

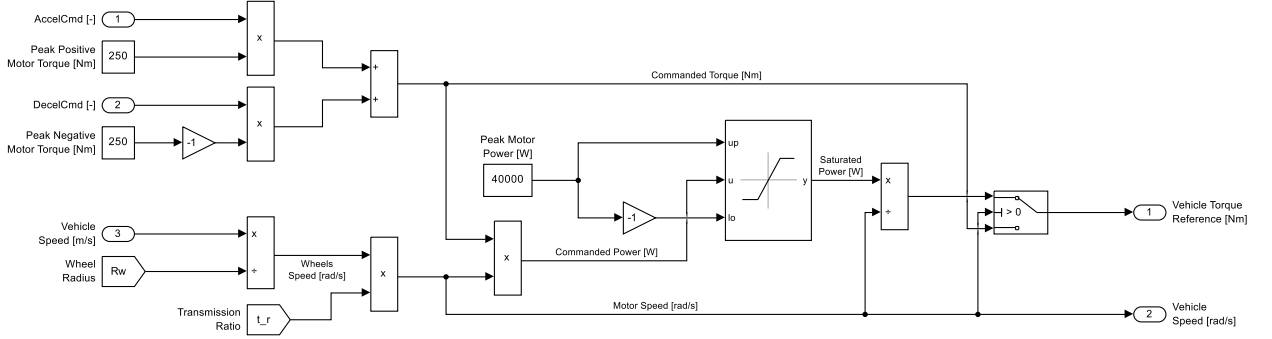


Fig. 3. Detail of the Motor Torque Reference Generation system.

In the proposed example the acceleration and deceleration signals, which are bounded between 0 and 1, are multiplied by the maximum motor torque and summed together. Then, the result is multiplied by the motor speed to obtain the motor power, which is then saturated to the maximum power capability of the motor. Finally, the saturated power signal is converted back into motor torque reference, T^* , before being outputted.

3.2. Generation of the stator flux limit signal

The flux management policy is the part of the motor control policy that is responsible for the calculation of the stator flux limit, $\lambda_{dqs,lim}$. It is based on two fundamental equations. The first provides an estimate of the maximum stator flux amplitude that the motor can be operated at, $\lambda'_{dqs,lim}$, while the second provides a correction coefficient called flux derating factor, FDF , whose value changes dynamically based on an inverter voltage saturation signal, V_{flag} , which is equal to 1 if the inverter is over the limit of linear operation (i.e., voltage saturation occurs) and is 0 if the inverter is within its linear operating region. Multiplying the estimated maximum flux amplitude by the correction coefficient, the actual stator flux limit, $\lambda_{dqs,lim}$, is obtained.

The stator flux amplitude, v_{dqs} , is the amplitude of the vector described by the Equation 3.

$$\begin{Bmatrix} v_{ds} \\ v_{qs} \end{Bmatrix} = R_s \begin{Bmatrix} i_{ds} \\ i_{qs} \end{Bmatrix} + \frac{d}{dt} \begin{Bmatrix} \lambda_{ds} \\ \lambda_{qs} \end{Bmatrix} + \omega \begin{bmatrix} 0 & -1 \\ 1 & 0 \end{bmatrix} \begin{Bmatrix} \lambda_{ds} \\ \lambda_{qs} \end{Bmatrix} \quad (3)$$

where ω is the motor synchronous speed, calculated as $\omega = p \omega_r$, with ω_r that is the rotor shaft speed and p the number of pole pairs.

Denoting as v'_{ds} and v'_{qs} the speed-independent terms of the expression of v_{ds} and v_{qs} respectively, Equation 4 can be obtained if the double product terms are neglected.

$$v_{dqs}^2 = v_{ds}'^2 + v_{qs}'^2 + \omega^2 \lambda_{dqs}^2 \quad (4)$$

The reason why the double product terms are not considered is that in most cases they are negligible with respect to the other terms of the equation. Reversing Equation 4 it is possible to obtain an expression for the stator flux as in Equation 5.

$$\lambda_{dqs} = \frac{1}{\omega} \sqrt{v_{dqs}^2 - v_{ds}'^2 - v_{qs}'^2} \quad (5)$$

The maximum flux limit at which the motor can operate is the one for which the inverter is at maximum voltage. Therefore, the following expressions holds, obtained by introducing Equation 2 into Equation 5.

$$\lambda'_{dqs,lim} = \frac{1}{\omega} \sqrt{(k_{mod} v_{DC} - \varepsilon_V)^2 - v'_{ds}{}^2 - v'_{qs}{}^2} \quad (6)$$

where ε_V is a small quantity set to avoid pushing the inverter to the absolute limit of its linear operating region.

The output of Equation 6, $\lambda'_{dqs,lim}$, is an estimate of the maximum stator flux amplitude at which the motor can be operated. Anyway, it is not possible to directly use it as an input signal for the LUTs because its value is an open-loop simplified estimate of the actual maximum feasible stator flux. The introduction of a corrective coefficient has proven to be an effective solution to close the loop with respect to DC voltage and eliminate the effect of modelling approximations, keeping the inverter in incipient voltage saturation conditions during flux weakening operation.

The dynamic equation of the flux derating factor, FDF , is:

$$F\dot{D}F = -k'_1 v_{flag} + k'_2 (1 - v_{flag}) \quad (7)$$

where V_{flag} is a flag signal that is equal to one when the inverter is at the limit of voltage saturation and zero otherwise. The expressions of k'_1 and k'_2 are:

$$k'_1 = \begin{cases} 0 & \text{if } FDF \leq 0 \\ k_1 & \text{if } FDF > 0 \end{cases} \quad (8)$$

$$k'_2 = \begin{cases} k_2 & \text{if } FDF \leq 1 \\ 0 & \text{if } FDF > 1 \end{cases} \quad (9)$$

where k_1 and k_2 are two tuning parameters, with $k_1 > 0$ and $k_2 > 0$.

Thanks to the formulation of k'_1 and k'_2 expressed in Equation 8 and Equation 9, the following condition is ensured:

$$0 < FDF \leq 1 \quad (10)$$

The value of the voltage flag signal, v_{flag} , is calculated according to the Equation 11.

$$v_{flag} = \begin{cases} 1 & \text{if } v_{dqs} \geq k_{mod} v_{DC} - \varepsilon_V \\ 0 & \text{if } v_{dqs} < k_{mod} v_{DC} - \varepsilon_V \end{cases} \quad (11)$$

Having both the preliminary flux limit, $\lambda'_{dqs,lim}$, and the flux derating factor, FDF , it is finally possible to calculate the stator flux limit signal, $\lambda_{dqs,lim}$:

$$\lambda_{dqs,lim} = FDF \lambda'_{dqs,lim} \quad (12)$$

4. Torque reference signal saturation process for single-motor single-ESS EV architectures

The inverter model receives the reference torque signal, T^* , and saturates it to guarantee compliance with the limitations on maximum power and voltage derived from Equation 1 and Equation 2. Additionally, the reference torque signal is saturated to the maximum (or minimum) feasible value at the imposed stator flux level.

A schematic representation of the saturation process is represented in Figure 4, where x_{ESS} is the state vector of the ESS, ω_m is the motor shaft speed, T_f is the flux-saturated torque reference, T_p is the power-saturated torque reference and T_v is the voltage-saturated torque reference.

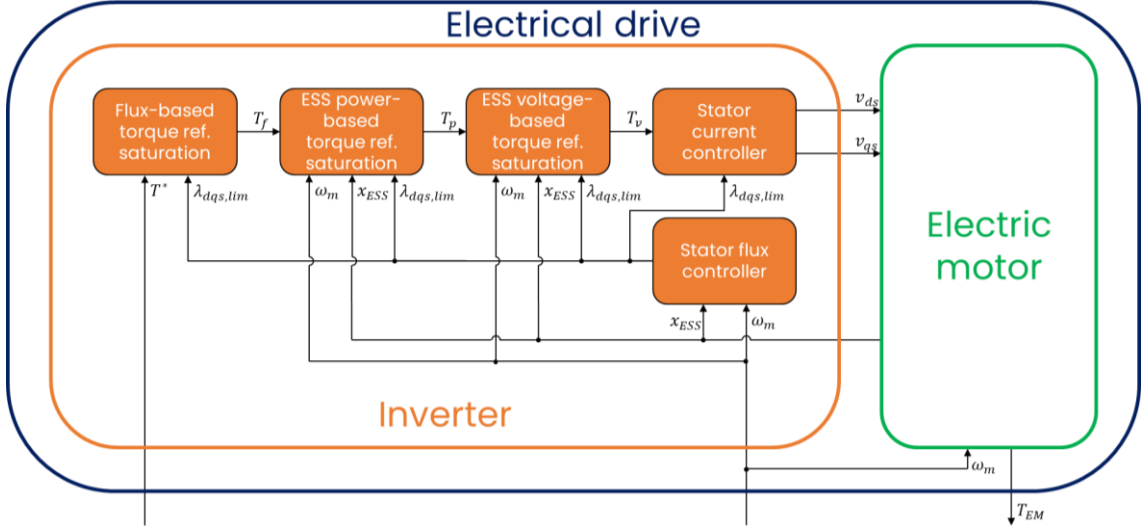


Fig. 4. Schematic representation of the electric drive model for single-motor EVs.

4.1. Flux-based torque reference saturation

The algorithm for LUT generation discretizes the motor operating domain and, for each possible operating condition, solves a numerical optimization problem to determine the best combination of d - and q -axis stator currents under the imposed constraints. Anyway, the algorithm is not always able to converge to a feasible solution under very demanding operating conditions, mainly at low stator flux limit and high torque values. To prevent the motor from operating under such conditions, the reference torque signal is saturated to the maximum (or minimum) feasible value for the imposed stator flux limit [56].

4.2. Power-based torque reference saturation

DC power-based torque reference saturation is necessary to avoid exceeding the maximum and minimum power that the ESS can deliver. Assuming to know the limit values for DC power, $P_{DC,max}$ and $P_{DC,min}$, it is possible to obtain the maximum and minimum power at the AC side of the inverter from Equation 1. In particular:

$$P_{AC,max} = \eta_{inv} P_{DC,max} \quad (13)$$

$$P_{AC,min} = \frac{1}{\eta_{inv}} P_{DC,min} \quad (14)$$

The role of the power saturator is to ensure that the AC power stays inside the feasible range, saturating the torque request if needed. To do so, it is necessary to estimate the stator-level motor power corresponding to the requested torque. This is accomplished by applying in sequence the LUTs and the motor model equations in order to convert the torque request into d - and q -axis stator currents, and the currents into stator-level power then.

The algorithm that performs the DC power-based torque reference saturation is based on the bisection search. The DC power corresponding to the flux-saturated torque reference is calculated first. If the power request falls within the feasible range, no power saturation of the torque reference signal is needed. Conversely, if the power request falls outside the feasible range, a dichotomic search is started to saturate the reference torque signal to the maximum (or minimum) feasible value. At each iteration the bisection routine tests a different torque value, gets the corresponding stator current components from the LUTs and calculates the corresponding stator-level power. The dichotomic search

is stopped when a torque value to which corresponds a DC power that is close enough to the corresponding DC power limit is found.

The use of a bisection search algorithm has proven to be computationally efficient, converging to a solution in few iterations, and flexible enough to allow its applications to different motor models. Indeed, dichotomic search algorithms are widely used in the literature to find the zeros of nonlinear problems [74].

4.3. Voltage-based torque reference saturation

DC voltage-based torque reference saturation is necessary to avoid exceeding the limit of linear operation of the inverter, which is expressed by Equation 2. The algorithm that accomplishes this task is conceptually very similar to the power saturator except for the fact that an additional bisection routine is necessary. Indeed, the algorithm converts the torque reference signal into d - and q - axis stator currents by means of the LUTs and then applies the motor model equations to calculate the corresponding stator power, P_{AC} , and voltage amplitude, V_{AC} . Then, the stator power is used to calculate the corresponding DC voltage by means of the ESS model equations.

The algorithm that performs the DC voltage-based torque reference saturation is based on two bisection routines nested one inside the other. The AC stator voltage and the DC voltage corresponding to the power-saturated torque reference are calculated first. If the limitation expressed by Equation 2 is respected, no voltage saturation of the torque reference signal is needed. Conversely, if the relationship expressed by Equation 2 is not respected, the algorithm starts the two-level dichotomic search to saturate the reference torque signal to the maximum (or minimum) feasible value. The bisection routine is stopped when a torque value to which corresponds an AC voltage that is close enough to the limit of inverter linear operation is found.

Figure 5 shows a schematic representation of the structure of the voltage saturation algorithm. At each iteration of the external bisection routine a different value of torque is tested, determining the corresponding stator power and voltage. Then, the internal bisection algorithm is run to determine the DC voltage corresponding to the tested torque level, using the stator power as input parameter. The DC voltage outputted by the internal bisection routine is then used to verify whether the limitation expressed by Equation 2 is respected or not.

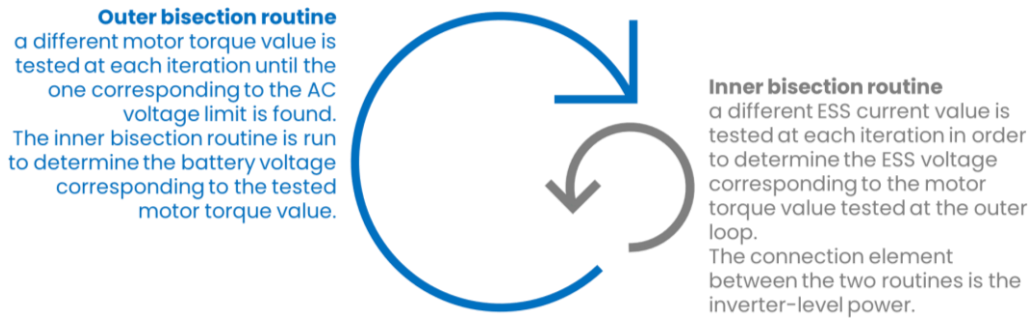


Fig. 5. Schematic representation of the voltage-based torque reference saturation algorithm.

5. Generalization of the torque reference signal saturation process to the case of multiple-motor EV architectures

The electric drive model structure presented in the previous paragraph is capable of propagating to the electric motor the limitations imposed by the ESS with high accuracy thanks to the use of the bisection algorithms for power and voltage saturation, which allow to efficiently find the solution of power-balance equations based on complex electric motor and ESS models. Anyway, this approach is not suitable for multiple-motor and/or multiple-ESS EV architectures, unless the property of the model of being 'plug-and-play' is lost.

It would in theory be possible to have the same modelling accuracy for multiple-motor and/or multiple-ESS EV architectures as for single-motor single-ESS ones, but this would require the need for heavy user modifications of the bisection search algorithms, featuring a detailed coded version of both the vehicle propulsion system and energy

storage system, which would make the model not plug-and-play. As a consequence, some conservative hypotheses have been made in order to make the inverter model plug-and-play for the case of multiple-motor and/or multiple-ESS EVs too:

- The power-based torque reference saturation is moved out of the electric drive model;
- The voltage-based torque reference saturation is simplified from a two-level bisection search to a single-level one, using a constant voltage threshold value (updated at each simulation timestep) instead of a detailed ESS model.

A schematic representation of the generalized torque reference saturation process is represented in Figure 6, where v_{DC} is the DC voltage threshold used in place of the ESS model. The fundamental idea behind the generalized model comes directly from the principle of conservation of energy. Assuming to have a powertrain composed of n electric drives and m ESSs, the total power absorbed by the n electric drives must be equal, considering the impact of inverters efficiency, to the total power delivered by the m ESSs. Since the total power is the variable that allows to connect the m ESSs to the n electric drives, having an Energy Management System (EMS) that can estimate at any instant of time the total power available from the ESSs and allocating such power to the individual electric drives is essential.

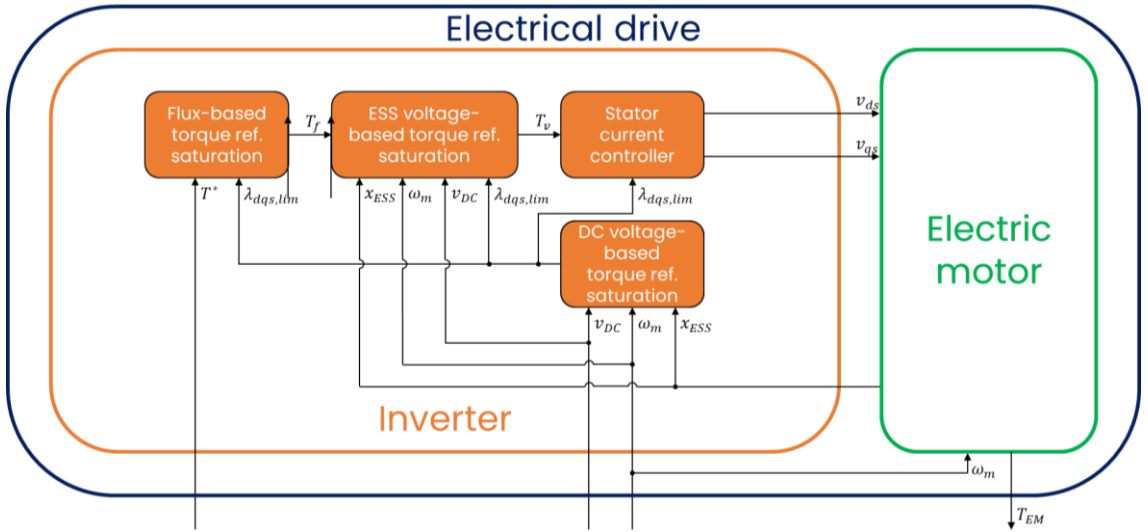


Fig. 6. Schematic representation of the generalized electrical drive model.

The EMS must be capable of:

- Acquiring information about the minimum and maximum power that each ESS can deliver individually;
- Acquiring information about the minimum and maximum power that each electric drive can absorb individually;
- Estimating the minimum and maximum power that the multi-ESS system can deliver as a whole;
- Estimating the minimum and maximum power that the propulsion system can absorb as a whole;
- Saturating the driver torque request to meet all the constraints on power;
- Acquiring torque reference signal for each individual electric drive;
- Acquiring voltage thresholds for each individual electric drive.

Figure 7 shows a schematical representation of the exchange of information between the ESSs and the electric drives through the EMS, where $P_{ESS,k}^{lim}$ is the vector containing the minimum and maximum power that the ESS k can deliver.

Thanks to the EMS, the structure of the generalized electric drive model can be greatly reduced with respect to that of the single-motor single-EES version. The need for user intervention is transferred from the electric drive model,

which remains plug-and-play, to the EMS, which is normally designed specifically for the application due to its vital role.

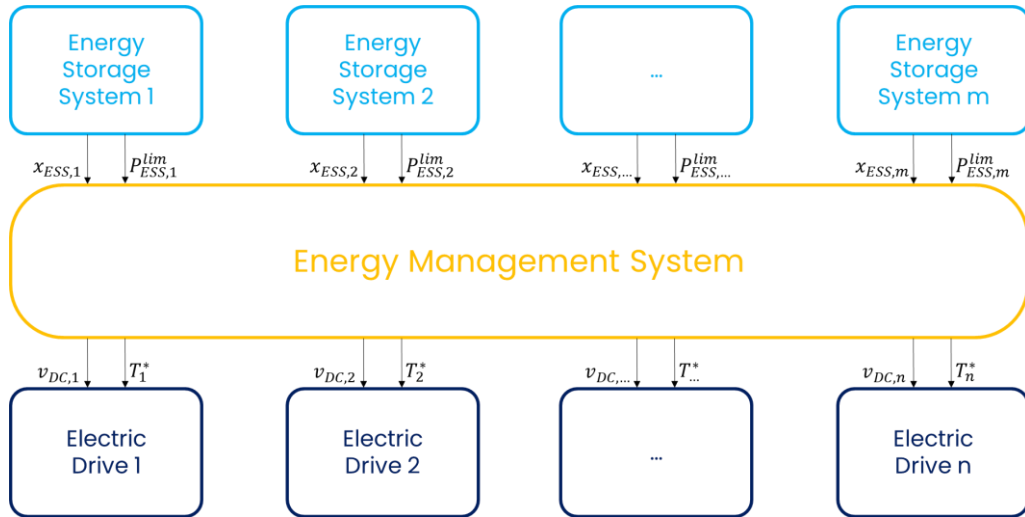


Fig. 7. Schematic representation of the role of the EMS as interface between the ESSs and the electric drives.

6. Generalized electric drive model validation

The results of an extensive work of validation of the PerfECT Design Tools, featuring the generalized version of the proposed inverter model, have been presented in [55]. An experimental campaign was conducted to gather data about the performance of the 2021 Long-Range AWD version of the Tesla Model 3 on three standard manoeuvres: 0-100-0 accelerations, double-lane change [81] (as per the ISO 3888-2 standard [82]) and constant-radius cornering.

The straight line 0-100-0 event was used to validate the longitudinal dynamics of the vehicle model. The trend of pedal position, DC bus current, DC bus voltage and DC bus power is reported in Figure 8, while that of speed and both front- and rear-axle motor torque can be found in [55].

A good correlation was obtained in terms of both shape and magnitude of all the parameters of interest with the observed curves recorded during the track tests. The following observations can be made:

- The simulated vehicle speed curve closely resembles the experimental one in terms of both accelerations and peak velocity. The main differences arise during the braking phase, with the experimental curves that shows a slightly better vehicle performance than the simulated one;
- Both the front- and rear-motor torque curves are very close to their experimental counterparts from Time=1 s to the end of the acceleration phase (Time=6 s). The simulated vehicle starts accelerating earlier but more gently than the actual car, but it then sharply increases the torque request to both the motors. All the differences between experimental and simulated curves vanish at Time=1 s;
- Some differences between the simulated and measured motor torque signals are observed in the braking phase. According to [55], they are due to the fact that the control policy implemented to rule the torque split between front- and rear-axle motors during regenerative braking events was not tuned to directly reflect the behaviour of the tested vehicle. This is also the cause of the slightly better braking performance of the real vehicle compared to the simulated one;
- The experimental motor torque signals show an oscillation at the end of the acceleration phase, between Time=5 s and Time=6 s. This is caused by the fact that the driver reduced the pressure on the acceleration pedal for a short time instant, causing an oscillation on the torque request and, consequently, on bus current, voltage and power;

- The simulated bus power curve shows a reduction between Time=5.5 s and Time=6.0 s caused. The cause of that is a torque and power derating algorithm implemented in a slightly more sophisticated version of the Motor Torque Reference Generation system shown in Figure 3. The thermal derating algorithm cuts the motor torque reference to prevent overheating phenomena.
- A very good correlation is found between the experimental and simulated signals of bus current, voltage and power signals during the entire duration of the braking maneuver.
- The most relevant differences between experimental and simulated bus current, voltage and power occur between Time=1 s and Time=4 s, period in which both motors are at maximum torque. This may be caused by the fact that the motor models used in the vehicle simulation cannot adequately describe motor behavior when the magnetic flux is very high. An in-depth dissertation about the motor models is available in [56]. This may be solved by means of a more detailed equivalent circuit motor model, which can easily be introduced in the simulation as demonstrated in [57]. Anyway, this would have required details about the motor performance that are not available to the authors.

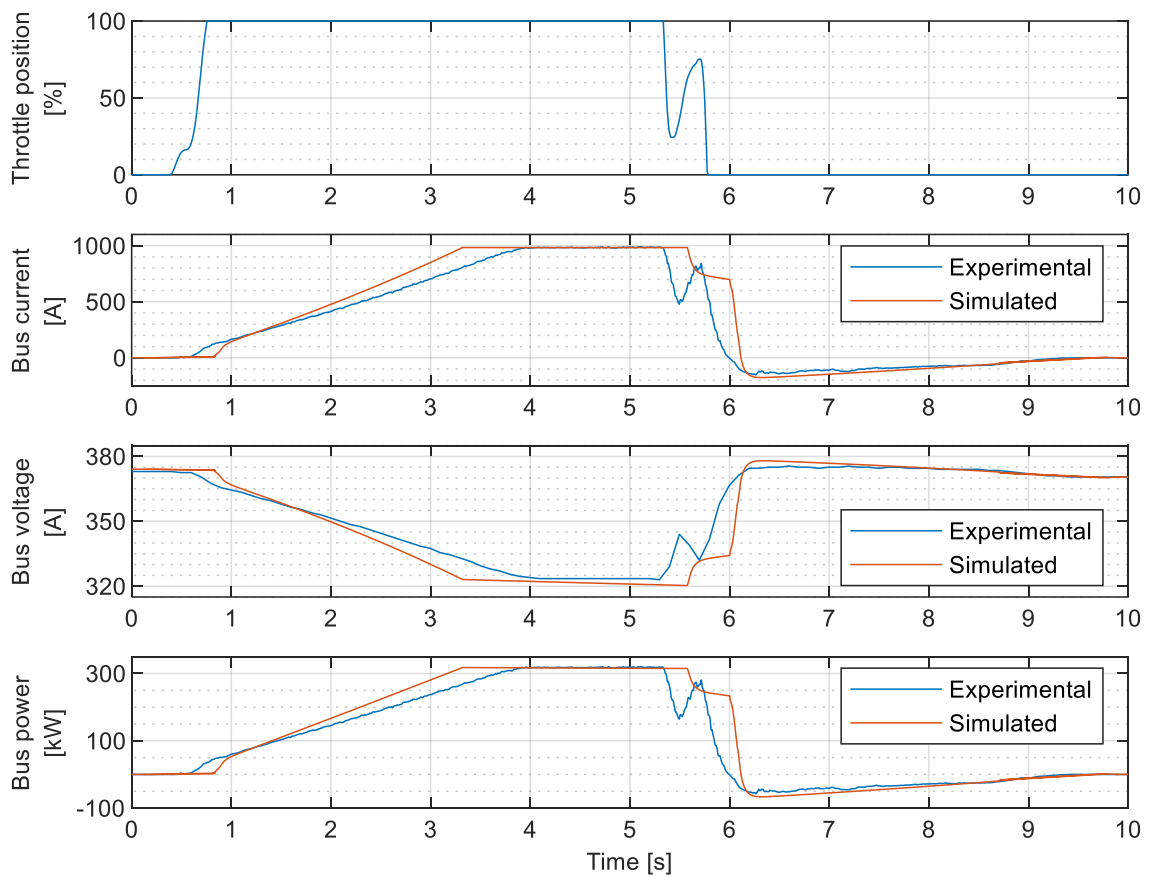


Fig. 8. Throttle position, bus current, bus voltage and bus power signals on a 0-100-0 manoeuvre.

7. Example of application in MATLAB/Simulink

This section proposes an example of practical application of the single-motor single-ESS version of the presented inverter model to demonstrate its effectiveness, showing the influence of the flux weakening policy on vehicle performance and highlighting how the torque reference saturation process can support engineers at correctly dimensioning the different powertrain components.

A vehicle model is created by using the data from the experimental test of the 2021 Long-Range AWD Tesla Model 3. An EMRAX 268 HV [83] is used to power the vehicle in place of its original electric drives to avoid modelling the EMS, which is out of the scope of this study. Since this example of application only focusses on vehicle performance in longitudinal direction, the lateral dynamics is not modelled. The main vehicle dimensional parameters are reported in Table 1 while the structure of the vehicle is shown in Figure 9.

Table 1. Main dimensional parameters of the simulated vehicle.

Parameter	Symbol	Value	Unit
Wheelbase	l	2875	mm
COG distance from the front axle	a	1419	mm
COG distance from the front axle	b	1456	mm

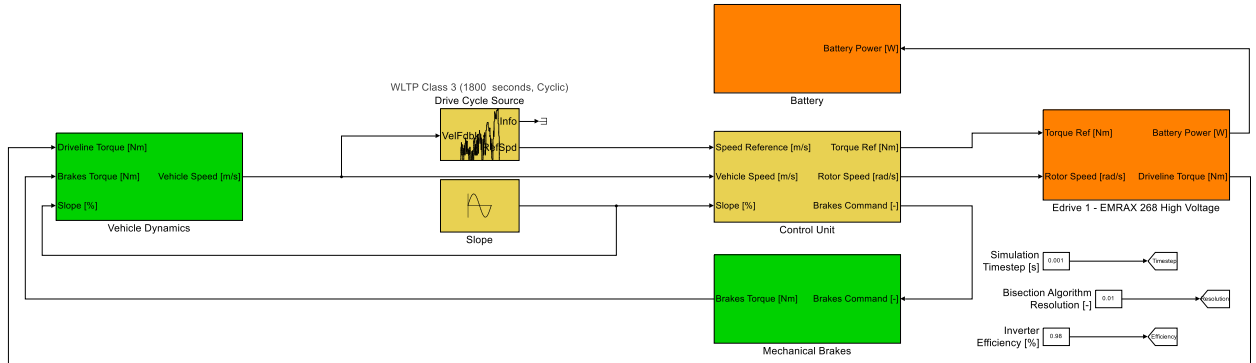


Fig. 9. Structure of the vehicle model.

7.1. Longitudinal vehicle dynamics

The driving resistance force, R_{dr} , to which a vehicle is subjected when travelling on a road with a slope α at a longitudinal velocity V is constituted of three components: aerodynamic drag, rolling resistance and grade force:

$$R_{dr} = R_{aero} + R_{roll} + R_{grad} \quad (15)$$

Aerodynamic drag force, R_{aero} , represents the dominant component of the driving resistance at high speeds. It represents the resistance that the air opposes to vehicle motion.

$$R_{aero} = \frac{1}{2} \rho S C_x V^2 \quad (16)$$

where ρ is the air density, S is the vehicle's frontal area and C_x is the vehicle's drag coefficient.

The rolling resistance force, R_{roll} , is the component of the total driving resistance due to the tires motion. It is mainly caused by the hysteresis of the tires elastomeric material that is repeatedly deformed and relaxed as tire rolls, but other minor phenomena contribute too [84].

$$R_{roll} = F_z (f_0 + k V^2) \quad (17)$$

where F_z is the vertical load acting on the tire and both f_0 and k are experimental coefficients.

The grade force, R_{grad} , is the component of vehicle weight in the direction parallel to the road:

$$R_{grad} = m g \sin(\alpha) \quad (18)$$

where m is the total vehicle mass and g is the gravity acceleration.

The total driving resistance is distributed between the four wheels of the vehicle, and it acts at the tires contact patch. The power that the motor should deliver to win driving resistance is greater than the driving resistance itself due to the presence of transmission losses in the kinematic chain that transfers power from the motor to the wheels. Transmission losses are generally modelled as an efficiency η_t which can be assumed as a constant for a first-approximation analysis:

$$P_{wheel} = \begin{cases} \eta_t P_{motor} & \text{if } P_{motor} \geq 0 \\ \frac{1}{\eta_t} P_{motor} & \text{if } P_{motor} < 0 \end{cases} \quad (19)$$

where P_{wheel} is the traction power delivered to the wheels.

The difference between the traction power at the wheels and the driving resistance power corresponds to the variation of the total kinetic energy of the vehicle and is thus the reason of accelerations and decelerations. Since several spinning masses are present in the vehicle powertrain, it is convenient to calculate an equivalent vehicle mass, m_e , which accounts for the contribution of the rotating masses to the total vehicle kinetic energy.

$$m_e = m + \frac{J_{wheel}}{R_e^2} + \frac{J_{trans}}{R_e^2 \tau_f^2} + \frac{J_{motor}}{R_e^2 \tau_f^2 \tau_g^2} \quad (20)$$

where τ_f is the transmission ratio of the final drive, τ_g is the transmission ration of the engaged gear, R_e is the effective rolling radius, J_{wheel} is the moment of inertia of the wheels, J_{trans} is the moment of inertia of the transmission and J_{motor} is the moment of inertia of the motor.

The longitudinal motion of the vehicle can be described according to Equation 21 and Equation 22:

$$\begin{cases} m \dot{V} = F_{x,1} + F_{x,2} + F_{x,aero} - m g \sin(\alpha) \\ F_{z,1} + F_{z,2} + F_{z,aero} - m g \cos(\alpha) = 0 \\ -m h_{CG} \dot{V} = F_{z,1} a - F_{z,2} b + m g h_{CG} \sin(\alpha) - M_{aer} + F_{x,aer} h_{CG} \end{cases} \quad (21)$$

$$\begin{cases} F_{z,1} = \frac{m g}{l} \left[b \cos(\alpha) - h_{CG} \sin(\alpha) - \frac{\rho S}{2 m g} (C_x h_{CG} - C_{M_y} l + b C_z) V^2 - \frac{h_{CG}}{g} \dot{V} \right] \\ F_{z,2} = \frac{m g}{l} \left[a \cos(\alpha) + h_{CG} \sin(\alpha) - \frac{\rho S}{2 m g} (-C_x h_{CG} + C_{M_y} l + a C_z) V^2 + \frac{h_{CG}}{g} \dot{V} \right] \end{cases} \quad (22)$$

where the subscripts 1 and 2 refers to the front and rear axle respectively. Further details can be found in [85, 86].

The main parameters of the longitudinal vehicle dynamic model are reported in Table 2.

Table 2. Main aerodynamic parameters of the simulated vehicle.

Parameter	Symbol	Value	Unit
Frontal area	S	2.22	m ²
Drag coefficient	C_x	0.23	-
Air density	ρ	1.225	kg/m ³

7.2. Electric drive

The electric drive model is based on three fundamental subsystems: Inverter, Motor and Driveline Torque Calculator. Its structure is shown in Figure 10.

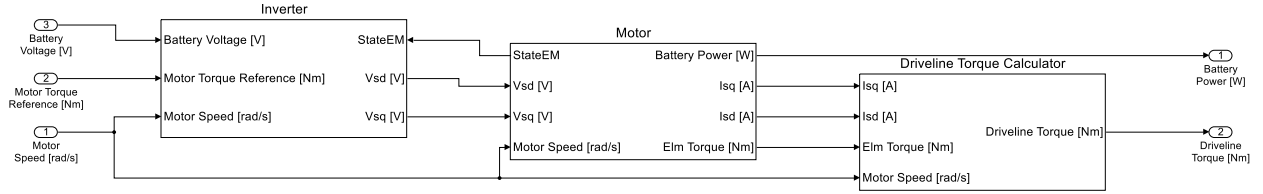


Fig. 10. Structure of the Electric Drive system.

The Inverter subsystem is based on the equations that have been presented in Section 2 and Section 3. Its structure is shown in Figure 11.

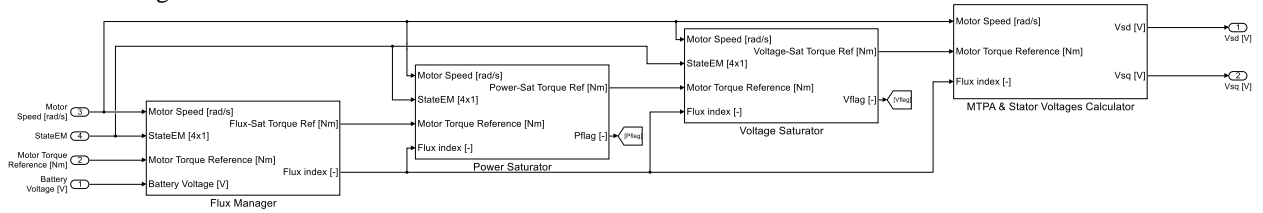


Fig. 11. Structure of the Inverter subsystem.

The inputs to the inverter subsystem are motor torque reference, T^* , motor speed, ω_m , motor state vector, x_{EM} , (featuring the d - and q -axis components of both stator current and stator flux) and battery voltage, v_{ESS} .

The first operation performed by the inverter subsystem is the calculation of the flux limit, which is based on Equation 6, Equation 7 and Equation 12. To reduce the complexity of the LUTs interpolation process, the flux limit, $\lambda_{dqs,lim}$, is converted to a flux index signal, λ_{idx} , which is the index of the element of the vector λ_s^V that is closest to $\lambda_{dqs,lim}$. After the flux index is obtained, the process of torque reference saturation occurs to ensure the compliance with stator flux, power and voltage constraints. The fully saturated torque reference, together with the flux index signal, is then used to generate the d - and q -axis stator current references, i_{ds}^* and i_{qs}^* , by interpolating the corresponding LUTs. Details about how the d - and q -axis LUTs of the EMRAX 268 HV have been obtained are available in [56].

The d - and q -axis stator current references, i_{ds}^* and i_{qs}^* , should be converted to stator voltage components, which are the ultimate output of the Inverter subsystem. Depending on the desired simulation accuracy, this can be done in three different ways:

- Under the assumption of having a perfect current controller, the actual stator current components perfectly track the references, thus $i_{ds} = i_{ds}^*$ and $i_{qs} = i_{qs}^*$. The d - and q -axis stator voltage components can therefore be obtained by applying the motor equivalent circuit model equations for stator voltages, which can generally be expressed in the form $v_{ds} = f_1(i_{ds}, \lambda_{ds}, \lambda_{qs})$ and $v_{qs} = f_2(i_{qs}, \lambda_{qs}, \lambda_{ds})$ [56];
- A closed-loop PI current controller based on the d - and q -axis stator currents feedback can be created [70, 71, 72] to generate the stator voltage reference signals, v_{ds}^* and v_{qs}^* . Assuming to have a perfect voltage controller, the actual stator voltages perfectly track the references thus $v_{ds} = v_{ds}^*$ and $v_{qs} = v_{qs}^*$;
- A closed-loop PI current controller based on the d - and q -axis stator currents feedback can be created [70, 71, 72] to generate the stator voltage reference signals, v_{ds}^* and v_{qs}^* . The inverter dynamics can then be simulated by means of a transfer function [87], thus $v_{ds} = G(v_{ds}^*)$ and $v_{qs} = G(v_{qs}^*)$.

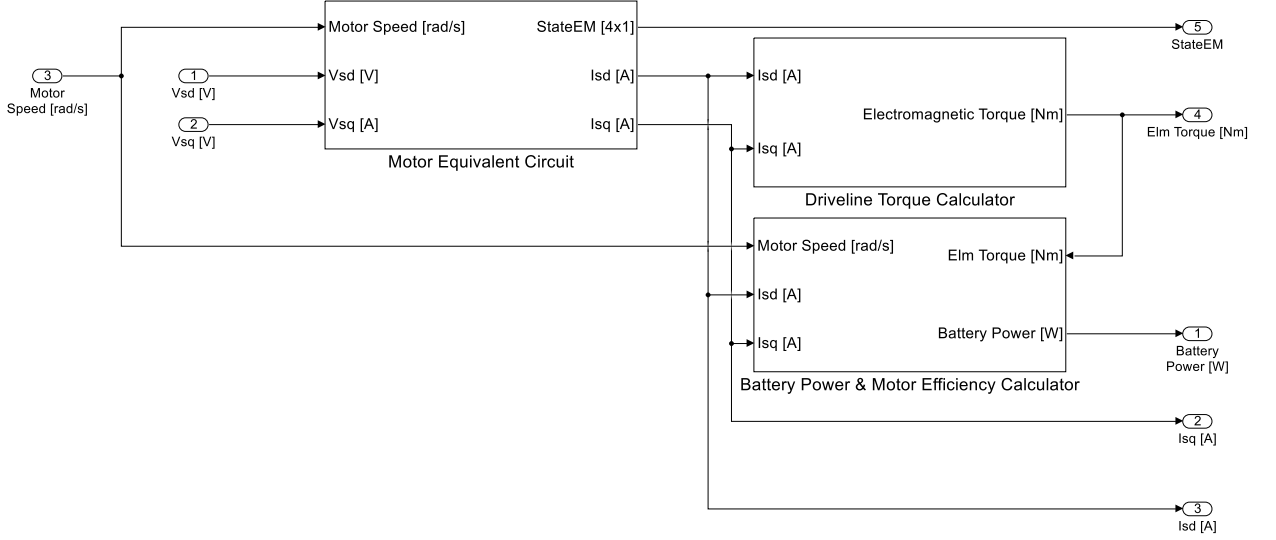


Fig. 12. Structure of the Motor subsystem.

Since the low-level dynamics of inverter control is not of interest for this case study, the first approach to stator voltage generation is selected. The stator voltage components, v_{ds} and v_{qs} , are output from the Inverter subsystem and fed to the Motor subsystem, whose structure is represented in Figure 12. It is composed of three different parts: Motor Equivalent Circuit, Electromagnetic Torque Calculator and Battery Power Calculator.

The Motor Equivalent Circuit block calculates the d - and q -axis stator currents, i_{ds} and i_{qs} , by reversing Equation 3. Being the EMRAX 268 HV synchronous, the generalized magnetic model for synchronous motors described by Equation 23 applies:

$$\begin{Bmatrix} \lambda_{ds} \\ \lambda_{qs} \end{Bmatrix} = \begin{bmatrix} L_d & 0 \\ 0 & L_q \end{bmatrix} \begin{Bmatrix} i_{ds} \\ i_{qs} \end{Bmatrix} + \begin{Bmatrix} \lambda_{md} \\ \lambda_{mq} \end{Bmatrix} \quad (23)$$

where L_d and L_q are respectively the d -axis and q -axis motor inductance, while λ_{md} and λ_{mq} are respectively the contributions of the permanent magnets to the d -axis and q -axis stator flux.

The values of λ_{md} and λ_{mq} change depending on the specific synchronous machine typology as described in Table 3, where λ_m represents the contribution of the permanent magnets to the stator flux. Further details about the magnetic model and the can be found in [56, 55].

Table 3. Contribution of the permanent magnets to the stator flux for different synchronous motor types [56].

Synchronous motor type	λ_{md}	λ_{mq}
Interior Permanent Magnet (IPM)	λ_m	0
Surface Permanent Magnet (SPM)	λ_m	0
Synchronous Reluctance (SyR)	0	0

The stator current components, i_{ds} and i_{qs} , are output from the Motor Equivalent Circuit block and fed to the Electromagnetic Torque Calculator, which applies Equation 24 to calculate the electromagnetic torque produced by the motor:

$$T_e = \frac{3}{2} p \bar{\lambda} \wedge \bar{i} = \frac{3}{2} p (\lambda_{ds} i_{qs} - \lambda_{qs} i_{ds}) \quad (24)$$

The parameters of the equivalent circuit model of the EMRAX 268 HV are reported in Table 4.

Table 4. EMRAX 268 HV equivalent circuit model parameters [83].

Parameter	Symbol	Value	Unit
Stator winding resistance	R_s	0.026	Ω
d -axis inductance	L_d	292	μH
q -axis inductance	L_q	273	μH
Permanent magnets flux	λ_m	0.1014	Vs
Number of pole pairs	p	10	-

The Battery Power Calculator block computes the power that the motor drains from the ESS based on the stator current components. The ESS power signal is then provided as an input to the ESS model.

The last element of the Inverter system is the Driveline Torque Calculator, a subsystem used to model the effect on the net torque output of the most relevant power dissipation phenomena that occur inside the electric motor. In this practical case, the motor equivalent circuit model described by Equation 23 only considers the effect of copper losses. Therefore, the Driveline Torque Calculator implements models for estimating iron losses, windage losses and bearing friction losses. The discussion about how these models are implemented is omitted for reasons of brevity, but details about it can be found in [55]. The output of the Driveline Torque Calculator is the net torque applied to the driveline by the motor.

7.3. Energy Storage System

The ESS of the simulated vehicle is a battery pack composed of four series-connected modules, resulting in an overall arrangement of 96 series and 46 parallels. The structure of the Simulink model of the vehicle traction battery is shown in Figure 13.

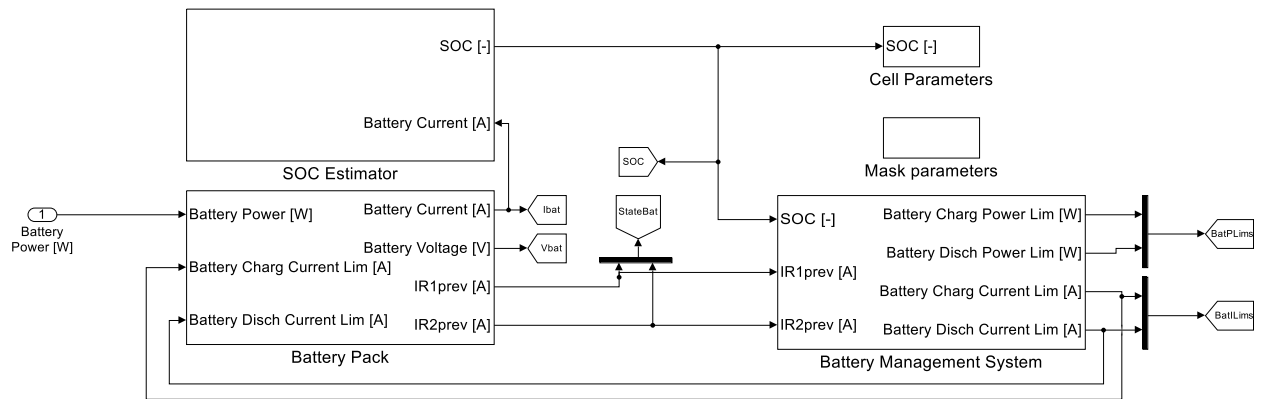


Fig. 13. Structure of the Battery subsystem.

The equivalent circuit diagram of choice to simulate the battery cells behavior is the dual polarization model shown in Figure 14, which is commonly encountered in the literature due to its ability to effectively describe battery cells dynamics by means of simple equations [59, 55, 73, 88, 29]. Six parameters are necessary to characterize the electrical behavior of a battery cell by means of the dual polarization model:

- Cell's open circuit voltage, $V_{OC,c}$;
- Cell's resistances, $R_{0,c}$, $R_{1,c}$ and $R_{2,c}$;
- Cell's capacitances, $C_{1,c}$ and $C_{2,c}$;

Depending on the desired level of accuracy, the battery parameters can be modelled as constant or as functions of cell's State of Charge (SoC) and temperature. In this practical example the cell's parameters are dependent on the SoC only, as shown in Table 5.

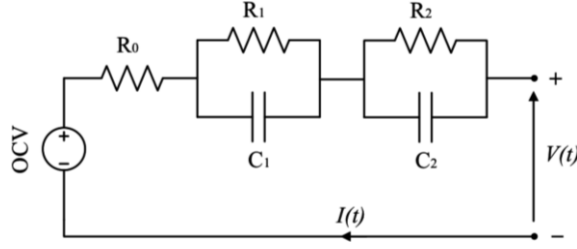


Fig. 14. Battery cell equivalent circuit diagram.

Table 5. EMRAX 268 HV equivalent circuit model parameters [83].

SoC	$R_{0,c}$ [Ω]	$R_{1,c}$ [Ω]	$R_{2,c}$ [Ω]	$C_{1,c}$ [F]	$C_{2,c}$ [F]	$V_{OC,c}$ [V]
0.00	0.0300	0.0066	0.0064	200	1000	2.75
0.10	0.0280	0.0064	0.0064	250	2500	2.96
0.20	0.0260	0.0072	0.0064	750	8500	3.17
0.30	0.0270	0.0072	0.0064	1100	12000	3.33
0.40	0.0250	0.0072	0.0064	1450	10000	3.53
0.50	0.0230	0.0080	0.0080	1650	15000	3.72
0.60	0.0240	0.0088	0.0096	1800	21500	3.88
0.70	0.0260	0.0088	0.0080	2000	15000	3.96
0.80	0.0270	0.0128	0.0096	2250	15000	4.08
0.90	0.0290	0.0240	0.0160	2100	22500	4.18

Considering the scheme in Figure 12, the cell voltage, v_c , is a function of the cell current, i_c .

$$v_c = v_{OC,c} - (R_{0,c} + R_{1,c} + R_{2,c}) i_c + R_{1,c} C_{1,c} \dot{v}_{RC1,c} + R_{2,c} C_{2,c} \dot{v}_{RC2,c} \quad (25)$$

where $\dot{v}_{RC1,c}$ is the time-derivative of the voltage across the network formed by the $R_{1,c}$, $C_{1,c}$ pair and $\dot{v}_{RC2,c}$ is the time-derivative of the voltage across the network formed by the $R_{2,c}$, $C_{2,c}$ pair.

The cell's SoC is calculated by means of equation 26:

$$SoC = SoC_0 - \frac{1}{Q_c} \int_{t_0}^t \eta_c i_c d\tau \quad (26)$$

where SoC_0 is the initial SoC, Q_c is the cell capacity and η_c is the cell's coulombic efficiency which, according to [73], can be approximated to 1 in the case of Li-ion cells.

Assuming all cells to be perfectly identical and denoting the number of series- and parallel-connected cells to form the pack as N_s and N_p respectively, the equivalent circuit diagram in Figure 12 can be extended to the entire pack by computing the pack-level equivalent circuit parameters as described by Equation 27:

$$V_{OC} = N_s V_{OC,c}, \quad Q = N_p Q_c, \quad R_j = \frac{N_s}{N_p} R_{j,c}, \quad C_k = \frac{N_p}{N_s} C_{k,c} \quad (27)$$

where $j = \{0,1,2\}$ and $k = \{1,2\}$.

Introducing the pack-level equivalent circuit parameters into Equation 25, the following expression for the battery voltage, v_{bat} , as a function of the battery current, i_{bat} is obtained:

$$v_{bat} = v_{OC} - (R_0 + R_1 + R_2) i_{bat} + R_1 C_1 \dot{v}_{RC1} + R_2 C_2 \dot{v}_{RC2} \quad (28)$$

The Battery Pack subsystem in Figure 11 implements a bisection search algorithm based on Equation 30 to find the battery voltage and current corresponding to the battery power request. At each iteration of the algorithm a different value of battery current is tested, and the search is stopped when the desired precision is obtained. The range of possible battery current values is bound by the charging and discharging current limits computed by the Battery Management System block, which calculates the maximum and minimum current and power level for which the constraints on cells SoC, voltage and current are respected [73, 74].

The SoC Estimator block in Figure 11 takes as input the battery current, i_{bat} , to compute the battery pack SoC according to Equation 29:

$$SoC = SoC_0 - \frac{1}{Q} \int_{t_0}^t \eta_c i_c dt \quad (29)$$

7.4. Simulation results

According to [83], the EMRAX 268 HV has continuous peak torque and power of 250 Nm and 40 kW respectively, and transient peak torque and power of 500 Nm and 160 kW respectively. Similarly, [55] states that Tesla Model 3's battery cells have a continuous peak current of 7.0 A and a transient peak current of 17.8 A. The exploitation of the overload capability of these powertrain components would cause the need to refine the vehicle control algorithm, overcomplicating the discussion without bringing any useful contribution. Because of this, the performance of all powertrain components is saturated to the limit of their continuous operation.

Figure 15 shows the speed profile of the vehicle on a wide-open throttle mission. The blue line shows the vehicle behavior when the stator flux is not weakened whereas the orange one represents the vehicle speed profile obtained by enabling the flux weakening policy.

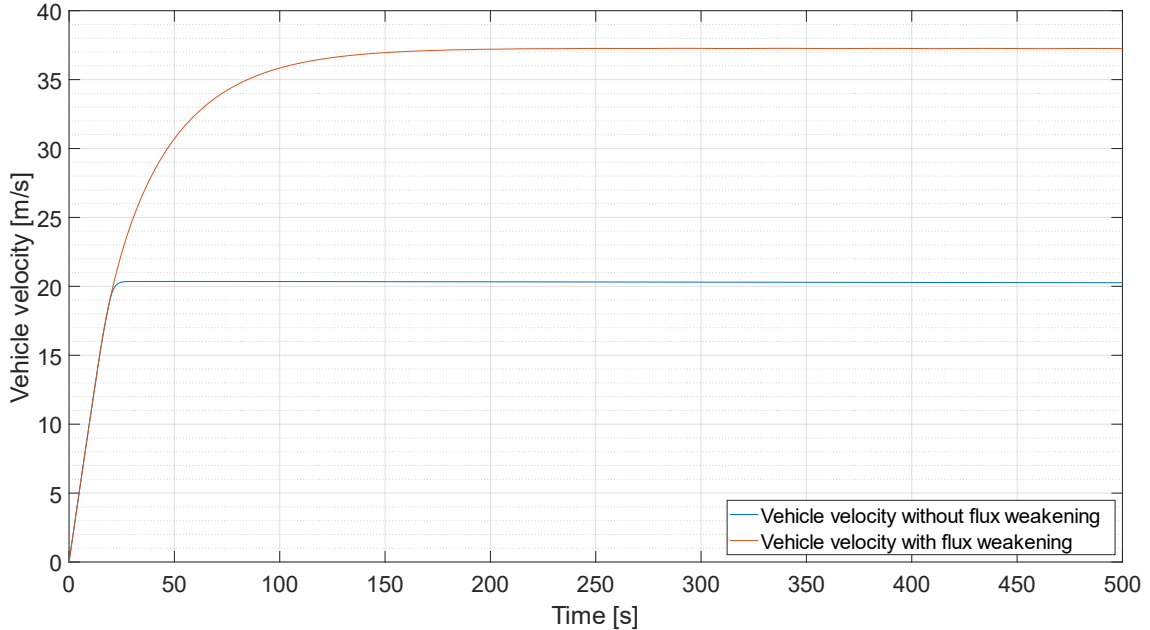


Fig. 15. Vehicle velocity profile with and without flux weakening.

As it is possible to see in Figure 15, in this specific case study the flux weakening policy allows to nearly double the top speed of the vehicle, evidencing the importance of being capable of modelling the effect that the DC voltage availability has on vehicle performance since the early stages of the design process. Additionally, the two different vehicle behaviors are obtained with the same hardware but with different control approaches, demonstrating the importance of the presented standardized motor control policy during vehicle design.

Figure 16 shows the stator voltage limit and the stator voltage amplitude when the flux weakening policy is enabled and when it is not. It is interesting to notice that in both cases the stator voltage sticks to its limit, but the reason for this is different not the same. When the flux control is not enabled, stator flux tracks the limit because of the action of the voltage-based torque reference saturator, which can effectively limit motor torque to respect the voltage limitation. When the flux weakening policy is enabled, the flux control algorithm is capable of keeping the motor in incipient voltage saturation conditions to fully exploit the voltage from the DC source.

The zoom in Figure 16 allows to appreciate the action of the flux weakening policy, which continuously adjusts the stator flux limit to track the stator voltage limit, resulting in oscillations of the stator voltage signals. The magnitude of these oscillations can be adjusted by tuning the parameters k_1 and k_2 in Equations 8 and Equation 9, and in the case of this example they remain bound within 1% of the stator voltage amplitude.

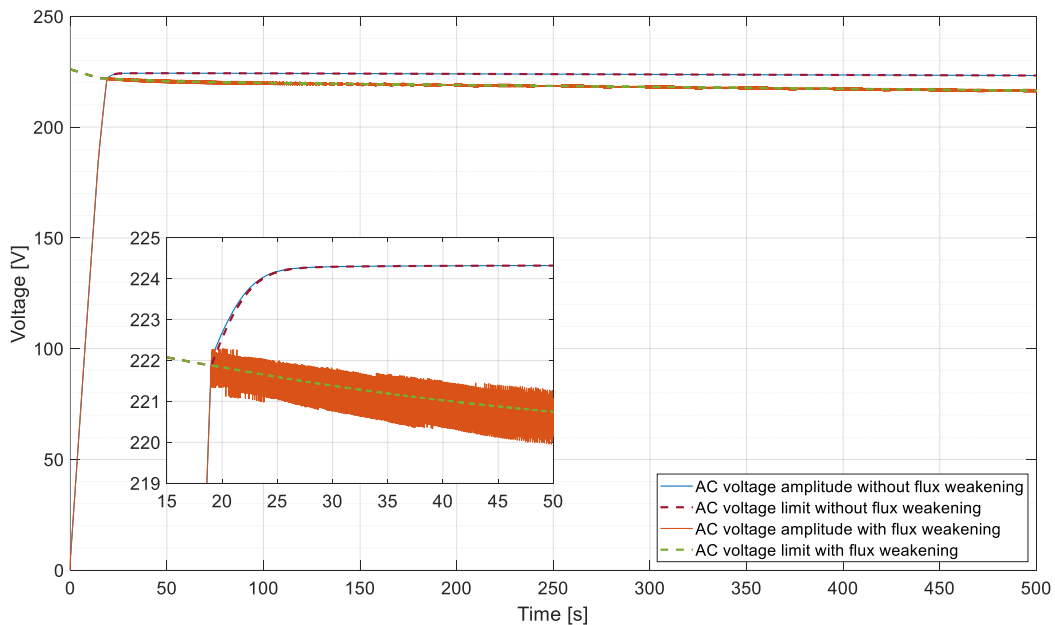


Fig. 16. Stator voltage limit and stator voltage amplitude with and without flux weakening.

The stator voltage limit is lower when the flux controller is enabled than when it is not because a higher current is drained from the battery to contrast the increased driving resistance that the vehicle encounters when its speed increases resulting, according to Equation 30, in a lower DC voltage.

Figure 17 shows the trend of the main variables of the flux weakening policy, obtained by setting $k_1 = 1$ and $k_2 = 1$. As it is possible to see, the differences between the preliminary flux limit and the derated flux limit are minimal, indicating that the preliminary flux limit value is a good estimate of the maximum flux that the motor can be operated at. The oscillations of the flux derating factor, which are quite small in magnitude, are the reason why the inverter is operated at the limit of its linear region. Indeed, the value of the flux derating factor is continuously increased and decreased based on the voltage saturation flag signal, oscillating around a steady state value after an initial overshoot.

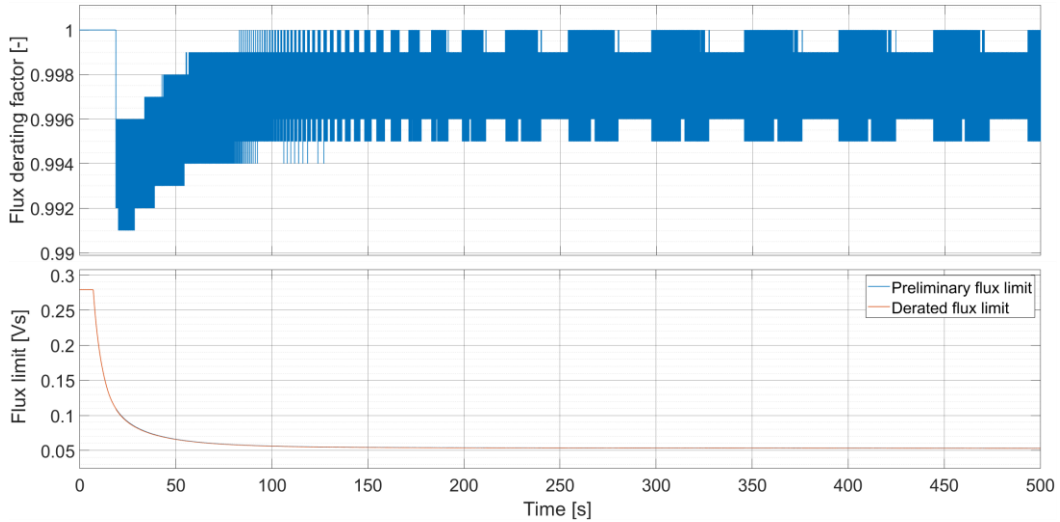


Fig. 17. Main variables of the flux weakening control policy.

While the effectiveness of the voltage saturation algorithm has been shown, that of the power saturator has not. To do it, the architecture of the battery layout of the vehicle has been changed to $N_s = 48$ and $N_p = 40$, greatly reducing its power output capabilities, and the vehicle has been simulated on the WLTP Class 3 cycle [89]. The evolution of the torque reference signal in such mission is shown in Figure 18.

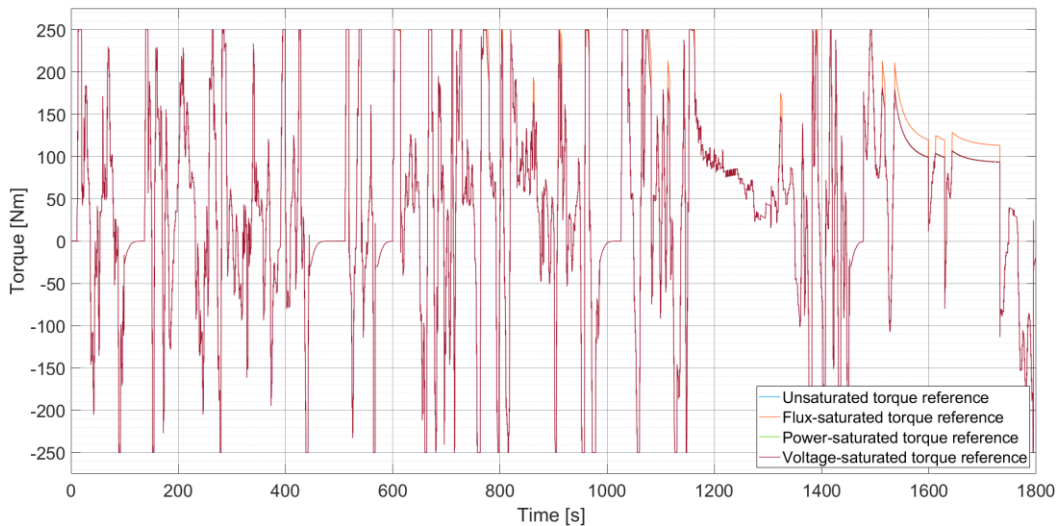


Fig. 18. Evolution of the torque reference signal on the WLTP Class 3 cycle.

The overlapping between the voltage-saturated torque reference curve and the power-saturated torque reference curve indicates that no voltage-based saturation of the torque reference signal occurs. Conversely, some spots are present where the power-saturated torque reference curve does not overlap to the flux saturated one, indicating the occurrence of power-based torque reference saturation events. This is confirmed by Figure 19, which shows the power request corresponding to both the flux-saturated and the power-saturated torque reference signals. As it is possible to see, the power-based torque reference saturation algorithm is capable of saturating the torque reference signal to match the limit of ESS operation.

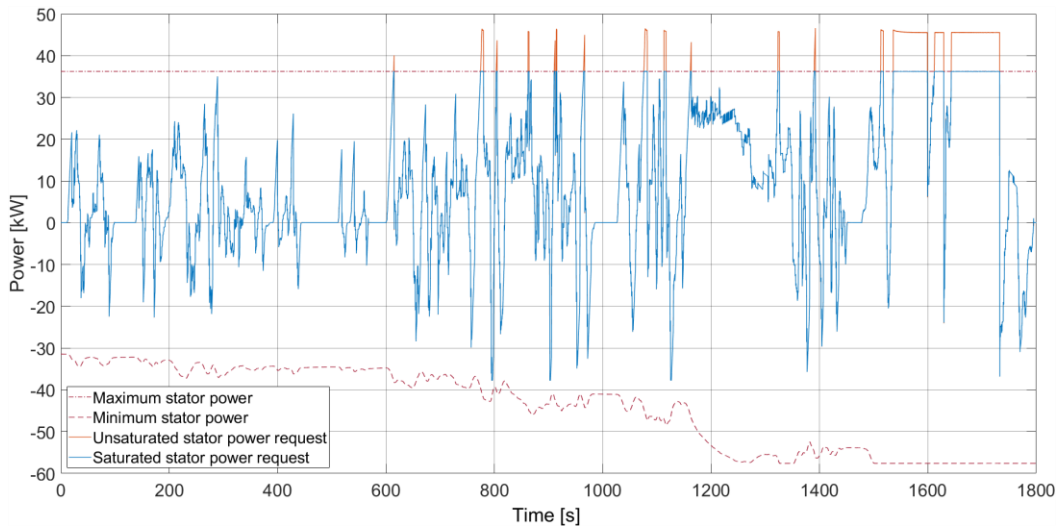


Fig. 19. Saturation of the stator power request on the WLTP Class 3 cycle.

The effect of the insufficient battery power availability on vehicle performance is well evident in Figure 20. Indeed, the vehicle is not capable of matching the reference speed profile on the extra-high section of the WLTP Class 3 cycle. Additionally, the insufficient battery power limits vehicle acceleration on some occasions, especially in the medium and high sections of the cycle.

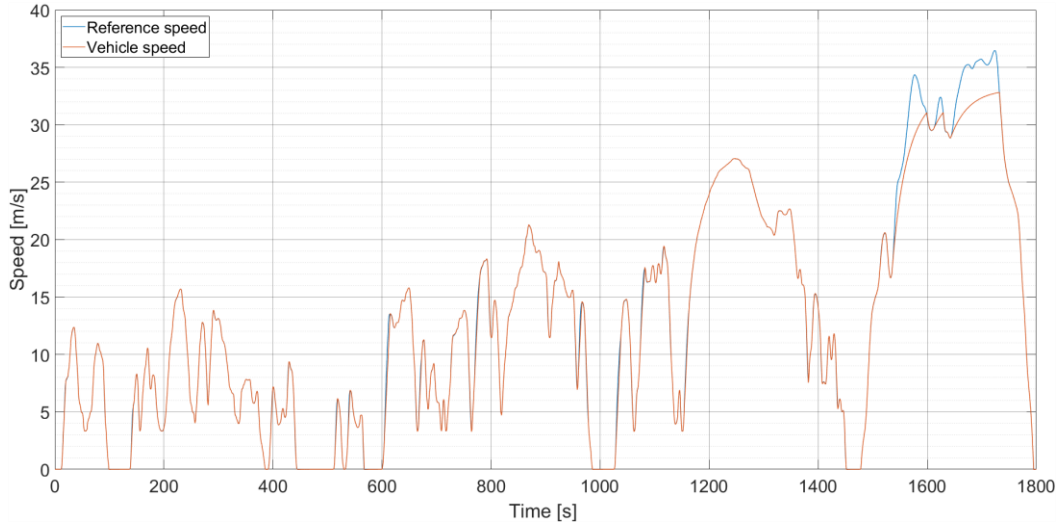


Fig. 20. Vehicle speed profile on the WLTP Class 3 cycle.

Figure 21 shows the battery energy output profiles for three different battery architectures, all featuring $N_p = 46$ but with different numbers of cells in series, $N_s = 96$, $N_s = 72$ and $N_s = 48$. The battery mass reduction obtained by reducing the value of N_s is estimated as a linear interpolation of the battery mass based as a function of the number of cells.

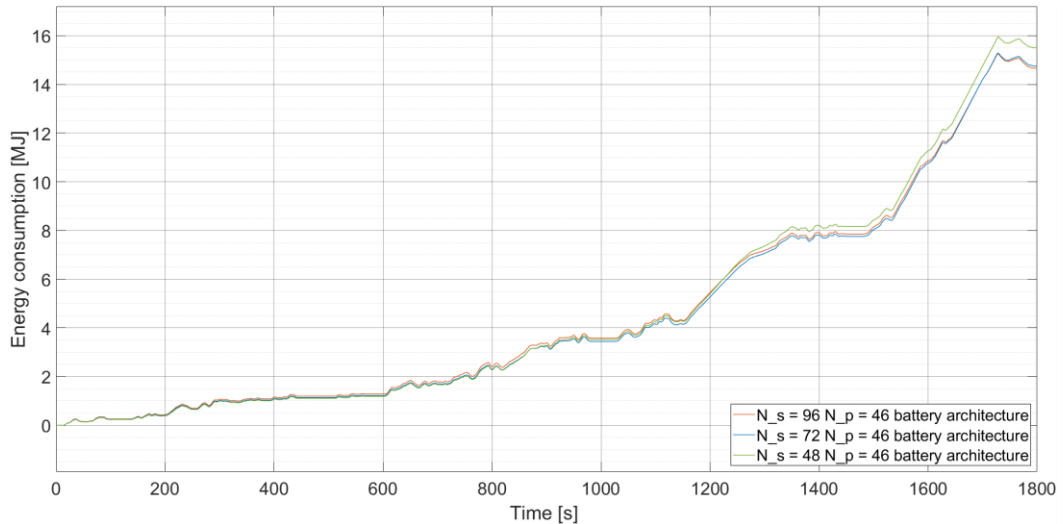


Fig. 21. Vehicle energy consumption on the WLTP Class 3 cycle.

This type of information allows to evaluate the trade-off between powertrain efficiency and battery mass. Indeed, a higher battery voltage brings to lower battery currents and reduced need to weaken the stator flux. Considering this, it is clear that the smallest-size battery pack is clearly under-dimensioned in terms of output voltage, bringing to a significantly increased energy consumption due to the need to greatly weaken stator flux in the high and extra-high sections of the WLTP Class 3 cycle. The other two architectures have similar energy consumptions over the cycle, considerably lower than that of the smallest size battery. The one with $N_s = 72$ shows a lower energy consumption in the low and medium sections of the WLTP Class 3 cycle than the $N_s = 96$ one due to its reduced mass, but this advantage is lost in the high and extra-high sections because of the increased need to weaken the stator flux.

8. Conclusions

A novel approach to electric drive modelling has been presented, based on an equivalent circuit description of the electric motor and a phenomenological inverter model. Embedding the low-level motor control within the LUTs enabled a significant reduction in model complexity and computational burden. Furthermore, the standardized flux weakening strategy that is implemented within the electric drive model allows for motor operation at different supply voltages, giving the possibility to analyze the influence of DC voltage on vehicle performance and energy consumption. The overall result is an electric drive modeling approach that offers a comprehensive yet efficient solution for investigating EV powertrains, providing valuable insights for vehicle design, optimization and performance analysis.

Two variants of the electric drive model are presented: a high-fidelity version for single-motor single-ESS EVs and a generalized version adaptable to multiple-motor and/or multiple-ESS EV architectures. Validation against experimental data from a Tesla Model 3 Long-Range AWD demonstrates the efficacy of the generalized model. Overall, the presented electric drive modelling approach has proven effective at predicting the evolution of the main electrical quantities along the powertrain of an AWD Tesla Model 3, implying its effectiveness as a tool for EVs simulations. Some differences between the simulated and recorded DC bus power signals have been found at the end of the constant-torque acceleration phase of the 0-100-0 test, apparently caused by a lower efficiency of the simulated electric drive with respect to the actual one. Since there was not the possibility to measure the d- and q-axis stator currents during the track test, it is impossible to trace the reason of these differences with absolute certainty. The most likely cause is the iron loss model, implemented as an add-on to the equivalent circuit motor models, which seems to overestimate the power loss when the motor operates under high speed and high stator flux, condition that is encountered at the end of the constant-torque acceleration phase, before flux is weakened. Unfortunately, the

implementation of a more accurate iron loss model requires input data that were not available to the authors. Anyway, those differences quickly vanished and a good correlation between simulated and recorded signal was found.

A simple case study has been presented and analyzed to show the capabilities of the presented inverter model, evidencing its effectiveness at saturating the torque reference signal to respect the limitations imposed by the power and voltage availability from the ESSs. The influence of the flux weakening policy on vehicle performance has been proven too, showing how it can greatly increase vehicle top speed and evidencing its impact on vehicle energy consumption.

Abbreviations

AC	Alternated Current
ADAS	Advanced Driver Assistance System
AWD	All-Wheel Drive
DC	Direct Current
ESS	Energy Storage System
EV	Electric Vehicle
GHG	Greenhous Gas
LCA	Life Cycle Assessment
LUT	LookUp Table
WLTP	Worldwide Harmonized Light-Duty Vehicles Test Procedure

References

- [1] Britannica, "Automobile — Early Electric Automobiles," [Online]. Available: <https://www.britannica.com/technology/automobile/Early-electric-automobiles>. [Accessed 25 January 2024].
- [2] J Turn Media, «What Was the Henney Kilowatt?», [Online]. Available: <https://blog.consumerguide.com/what-was-the-henney-kilowatt>. [Accessed 25 January 2024].
- [3] California Air Resources Board, "Zero-Emission Vehicle Program," [Online]. Available: <https://ww2.arb.ca.gov/our-work/programs/zero-emission-vehicle-program>. [Accessed 25 January 2024].
- [4] European Economic Community, «EEC Council Directive 91/441», [Online]. Available: <https://eur-lex.europa.eu/legal-content/EN/TXT/?uri=celex%3A31991L0441>. [Accessed 25 January 2024].
- [5] European Commission, «Q&A: Commission Proposal on the New Euro 7 Standards», [Online]. Available: https://ec.europa.eu/commission/presscorner/detail/en/qanda_22_6496. [Accessed 25 January 2024].
- [6] European Parliament, "Fit for 55: Zero CO2 Emissions for New Cars and Vans in 2035," [Online]. Available: <https://www.europarl.europa.eu/news/en/press-room/20230210IPR74715/fit-for-55-zero-co2-emissions-for-new-cars-and-vans-in-2035>. [Accessed 25 January 2024].
- [7] European Parliament, «Deal Confirms Zero-Emissions Target for New Cars and Vans in 2035,» [Online]. Available: <https://www.europarl.europa.eu/news/en/press-room/20221024IPR45734/deal-confirms-zero-emissions-target-for-new-cars-and-vans-in-2035>. [Accessed 25 January 2024].
- [8] G. Berdichevsky, K. Kelty, J. Straubel and E. Toomre, «The Tesla Roadster Battery System», [Online]. Available: <http://large.stanford.edu/publications/power/references/docs/tesla.pdf>. [Accessed 25 January 2024].
- [9] G. E. Blomgren, «The Development and Future of Lithium Ion Batteries», *Journal of The Electrochemical Society*, vol. 164, n. 1, 2016, doi: 10.1149/2.0251701jes.
- [10] J. T. Frith, M. J. Lacey and U. Ulissi, «A non-academic perspective on the future of lithium-based batteries», *Nature Communications*, vol. 14, n. 420, 2023, doi: 10.1038/s41467-023-35933-2
- [11] Statista, «Electric Vehicles—Worldwide», [Online]. Available: <https://www.statista.com/outlook/mmo/electric-vehicles/worldwide>. [Accessed 25 January 2024].
- [12] Allied Market Research, «Electric Vehicle Market Share, Size, Analysis», [Online]. Available: <https://www.alliedmarketresearch.com/electric-vehicle-market>. [Accessed 25 January 2024].
- [13] F. Hao, X. Lu, Y. Qiao and X. Chen, «Crashworthiness Analysis of Electric Vehicle With Energy-Absorbing Battery Modules», *J. Eng. Mater. Technol.*, 2017.

- [14] S. Kang, M. Kwon, J. Yoon Choi and S. Choi, «Full-scale fire testing of battery electric vehicles», *Applied Energy*, vol. 332, 2023, doi: 10.1016/j.apenergy.2022.120497.
- [15] S. Kim, J. Lee and C. Lee, «Does Driving Range of Electric Vehicles Influence Electric Vehicle Adoption?», *Sustainability*, vol. 9, n. 10, p. 1783, 2017, doi: 10.3390/su9101783.
- [16] N. Andrenacci and M. P. Valentini, «A Literature Review on the Charging Behaviour of Private Electric Vehicles», *Applied Sciences*, vol. 13, n. 23, p. 12877, 2023, doi: 10.3390/app132312877.
- [17] L. Kumar and N. Ravi, «Electric vehicle charging method and impact of charging and discharging on distribution system: A review», *Int. J. Electric and Hybrid Vehicles*, vol. 14, pp. 87-111, 2022, doi: 10.1504/IJEHV.2022.125253.
- [18] J. Dong and Z. Lin, «Within-day recharge of plug-in hybrid electric vehicles: Energy impact of public charging infrastructure», *Transportation Research Part D: Transport and Environment*, vol. 17, pp. 405-412, 2012, doi: 10.1016/j.trd.2012.04.003.
- [19] S. Ahmed, P. A. Nelson, K. G. Gallagher, N. Susarla and D. W. Dees, «Cost and energy demand of producing nickel manganese cobalt cathode material for lithium ion batteries», *Journal of Power Sources*, vol. 342, n. 28, pp. 733-740, 2017, doi: 10.1016/j.jpowsour.2016.12.069.
- [20] P. W. Gruber, P. A. Medina and G. A. Keoleian, S. E. Kesler, M. P. Everson, T. J. Wallington, «Global Lithium Availability», *Journal of industrial ecology*, 2011, doi: 10.1111/j.1530-9290.2011.00359.x.
- [21] X. Huang, Y. Lin, F. Liu, M. K. Lim and L. Li, «Battery Recycling Policies for Boosting Electric Vehicle Adoption: Evidence from a Choice Experimental Survey», vol. 24, pp. 2607-2620, 2022, doi: 10.1007/s10098-022-02340-y.
- [22] G. P. Nong and S. L. Pang, «Research on the Electric Vehicle Remanufacturable Battery Supply Chain with Recycling Channels», *Advanced Materials Research*, vol. 773, p. 948–953, 2013, doi: 10.4028/www.scientific.net/AMR.773.948.
- [23] S. Feng, «System dynamics model for battery recycling of electric vehicles in Anylogic simulateon», *International Journal of Internet Manufacturing and Services*, vol. 5, n. 4, pp. 405-418, 2018, doi: 10.1504/IJIMS.2018.095260.
- [24] F. Rieck, K. Machielse and R. van Duin, «Will Automotive Be the Future of Mobility?», *World Electric Vehicle Journal*, vol. 11, n. 1, 2022, doi: 10.3390/wevj11010010.
- [25] H. d. Carvalho Pinheiro, A. Messana, L. Sisca, A. Ferraris, A. G. Airale and M. Carello, «Torque Vectoring in Electric Vehicles with In-wheel», in *15th IFToMM World Congress on Mechanism and Machine Science*, KrackoW, 2019, doi: 10.1007/978-3-030-20131-9_308.
- [26] G. Gebresilassie Eshetu, H. Zhang, X. Judez, H. Adenusi, M. Armand, S. Passerini and E. Figgemeier, «Production of high-energy Li-ion batteries comprising silicon-containing anodes and insertion-type cathodes», *Nature Communications*, vol. 12, 2021, doi: 10.1038/s41467-021-25334-8.
- [27] A. Varzi, R. Raccichini, S. Passerini and B. Scrosati, «Challenges and prospects of the role of solid electrolytes in the revitalization of lithium metal batteries», *Journal of Materials Chemistry A*, vol. 4, pp. 17251-17259, 2016, doi: 10.1039/C6TA07384K.
- [28] M. H. Braga, N. S. Grundish, A. J. Murchison and J. B. Goodenough, «Alternative strategy for a safe rechargeable battery», *Energy & Environmental Science*, vol. 10, pp. 331-336, 2017, doi: 10.1039/C6EE02888H.
- [29] A. Rizzello, S. Scavuzzo, A. Ferraris, A. G. Airale, E. Bianco and M. Carello, «Non-linear Kalman Filters for Battery State of Charge Estimation and Control», in *2021 International Conference on Electrical, Computer, Communications and Mechatronics Engineering (ICECCME)*, Mauritius, 2021, doi: 10.1109/ICECCME52200.2021.9590976.
- [30] J. Christensen, P. Albertus, R. S. Sanchez-Carrera, T. Lohmann, B. Kozinsky, R. Liedtke, J. Ahmed and A. Kojic, «A Critical Review of Li/Air Batteries», *Journal of The Electrochemical Society*, vol. 159, n. 2, 2011, doi: 10.1149/2.086202jes.
- [31] H. Wang, Y. Yang, Y. Liang, J. T. Robinson, Y. Li, A. Jackson, Y. Cui and H. Dai, «Graphene-Wrapped Sulfur Particles as a Rechargeable Lithium–Sulfur Battery Cathode Material with High Capacity and Cycling Stability», *Nano Letters*, vol. 11, n. 7, pp. 2644-2647, 2011, doi: 10.1021/nl200658a.
- [32] X. Ji, K. T. Lee and L. F. Nazar, «A highly ordered nanostructured carbon–sulphur cathode for lithium–sulphur batteries», *Nature Materials*, vol. 8, pp. 500-506, 2009, doi: 10.1038/nmat2460.
- [33] P. Hartmann, C. L. Bender, J. Sann, A. K. Dürr, M. Jansen, J. Janek and P. Adelhelm, «A comprehensive study on the cell chemistry of the sodium superoxide (NaO₂) battery», *Physical Chemistry Chemical Physics*, vol. 15, p. 11661–11672, 2013, doi: 10.1039/C3CP50930C.
- [34] P. Hartmann, C. L. Bender, M. Vračar, A. K. Dürr, A. Garsuch, J. Janek and P. Adelhelm, «A rechargeable room-temperature sodium superoxide (NaO₂) battery», *Nature Materials*, vol. 12, p. 228–232, 2013, doi: 10.1038/nmat3486.
- [35] Hitachi Zosen Corporation, «All-Solid-State Lithium-Ion Batteries,» [Online]. Available: <https://www.hitachizosen.co.jp/english/business/field/functional/as-lib.html>. [Accessed 26 January 2024].
- [36] Y. Duan, X. Bai, T. Yu, Y. Rong, Y. Wu, X. Wang, J. Yang and J. Wang, «Research progress and prospect in typical sulfide solid-state electrolytes», *Journal of Energy Storage*, vol. 55, p. 105382, 2022, doi: 10.1016/j.est.2022.105382.
- [37] N. Suzuki, T. Watanabe, S. Fujiki and Y. Aihara, «Solid-State Batteries with Inorganic Electrolytes», in *Batteries: Present and Future Energy Storage Challenges*, Wiley, 2022, p. 1–62.

- [38] E. Bianco, L. Di Napoli, E. Grano and M. Carello, «E-scooter modelling: battery and fuel cell system integration», in *The Fourth International Conference of IFToMM Italy*, Napoli, 2022, doi: 10.1007/978-3-031-10776-4_104.
- [39] C. Cubito, L. Rolando, A. Ferraris, M. Carello and F. Millo, «Design of the control strategy for a range extended hybrid vehicle by means of dynamic programming optimization», in *IEEE Intelligent Vehicles Symposium*, Los Angeles, 2017, doi: 10.1109/IVS.2017.7995881
- [40] H. d. Carvalho Pinheiro, G. Imberti and M. Carello, «Pre-Design and Feasibility Analysis of a Magneto-Rheological Braking System for Electric Vehicles», in *SAE 2023 World Congress Experience, WCX 2023*, Detroit, 2023, doi: 10.4271/2023-01-0888.
- [41] T. Lažek, I. Pazdera and M. Toman, «Comparison and Simulation of Two Loss Minimization Algorithms for Field-oriented Control of Induction Motor», in *2022 IEEE 20th International Power Electronics and Motion Control Conference (PEMC)*, Brasov, 2022, doi: 10.1109/PEMC51159.2022.9962920.
- [42] T. Lažek, I. Pazdera and M. Toman, «Simulation and Comparison of a Loss Minimization Algorithm with Conventional Efficiency Improvement Methods for Field-Oriented Control of an Induction Machine», in *2023 IEEE International Conference on Environment and Electrical Engineering and 2023 IEEE Industrial and Commercial Power Systems Europe (EEEIC / I&CPS Europe)*, Madrid, 2023, doi: 10.1109/EEEIC/ICPSEurope57605.2023.10194662.
- [43] S. A. Odhano, R. Bojoi, A. Boglietti, S. G. Rosu and G. Griva, «Maximum efficiency per torque direct flux vector control of induction motor drives», *IEEE Transactions on Industry Applications*, vol. 51, n. 6, pp. 4415 - 4424, 2015, doi: 10.1109/TIA.2015.2448682.
- [44] S. Rubino, D. Obrad, R. Bojoi and E. Levi, «Modular Vector Control of Multi-Three-Phase Permanent Magnet Synchronous Motors», *IEEE Transactions on Industrial Electronics*, vol. 68, n. 10, pp. 9136 - 9147, 2021, doi: 10.1109/TIE.2020.3026271.
- [45] E. Bianco, S. Rubino, M. Carello and I. R. Bojoi, «Advanced Torque Control of Interior Permanent Magnet Motors for Electrical Hypercars», *World Electric Vehicle Journal*, vol. 15, n. 2, 2023, doi: 10.3390/wevj15020046.
- [46] P. Girardi, A. Gargiulo and P. C. Brambilla, «A comparative LCA of an electric vehicle and an internal combustion engine vehicle using the appropriate power mix: The Italian case study», *The International Journal of Life Cycle Assessment*, vol. 20, p. 1127–1142, 2015, doi: 10.1007/s11367-015-0903-x.
- [47] S. R. Deshpande, S. Gupta, D. Kibalama, N. Pivaro and M. Canova, «Benchmarking Fuel Economy of Connected and Automated Vehicles in Real World Driving Conditions via Monte Carlo Simulation», in *ASME 2020 Dynamic Systems and Control Conference*, 2020, doi: 10.1115/DSCC2020-3250.
- [48] S. Gupta, S. R. Deshpande, D. Tufano, M. Canova, G. Rizzoni, K. Aggoune, P. Olin and J. Kirwan, «Estimation of Fuel Economy on Real-World Routes for Next-Generation Connected and Automated Hybrid Powertrains», in *2020 SAE World Congress Experience, WCX 2020*, 2020, doi: 10.4271/2020-01-0593.
- [49] P. Plin, K. Aggoune, L. Tang, K. Confer, J. Kirwan, S. R. Deshpande, S. Gupta, P. J. Tulpule, M. Canova and G. Rizzoni, «Reducing Fuel Consumption by Using Information from Connected and Automated Vehicle Modules to Optimize Propulsion System Control», in *2019 SAE World Congress Experience, WCX 2019*, Detroit, 2019, doi: 10.4271/2019-01-1213.
- [50] Tesla, «Go Anywhere.» [Online]. Available: <https://www.tesla.com/trips>. [Accessed 26 January 26].
- [51] Volkswagen, «E-Route Planner.» [Online]. Available: <https://www.volkswagen.it/it/auto-elettriche-e-ibride/ricarica-e-autonomia/e-route-planner.html>. [Accessed 26 January 2024].
- [52] Porsche, «Porsche E-Performance.» [Online]. Available: <https://www.porsche.com/international/aboutporsche/e-performance>. [Accessed 26 January 2024].
- [53] S. Schoenberg and F. Dressler, «Reducing Waiting Times at Charging Stations with Adaptive Electric Vehicle Route Planning», in *IEEE Transactions on Intelligent Vehicles*, vol. 8, p. 95–107, 2023, doi: 10.1109/TIV.2022.3140894.
- [54] A. Ponso, A. Bonfitto and G. Belingardi, «Route Planning for Electric Vehicles Including Driving Style, HVAC, Payload and Battery Health», *Energies*, vol. 16, n. 12, 2023, doi: 10.3390/en16124627.
- [55] H. d. Carvalho Pinheiro, «PerfECT Design Tool: Electric Vehicle Modelling and Experimental Validation», *World Electric Vehicle Journal*, vol. 14, n. 12, 2023, doi: 10.3390/wevj14120337.
- [56] E. Grano, E. Bianco, H. d. Carvalho Pinheiro and M. Carello, «MTPA and flux weakening control of electric motors: a numerical approach», in *2023 IEEE International Conference on Environment and Electrical Engineering and 2023 IEEE Industrial and Commercial Power Systems Europe (EEEIC / I&CPS Europe)*, Madrid, 2023, doi: 10.1109/EEEIC/ICPSEurope57605.2023.10194684.
- [57] E. Grano, T. Lazek and M. Carello, «A numerical methodology for induction motor control: lookup tables generation and steady-state performance analysis», in *SAE World Congress Experience (WCX24)*, Detroit, 2024, doi: 10.4271/2024-01-2152.
- [58] Cambridge University Press & Assessment, «Cambridge Dictionary - Phenomenology.» [Online]. Available: <https://dictionary.cambridge.org/us/dictionary/english/phenomenology>. [Accessed on 4 June 2024].
- [59] E. Bianco, A. Rizzello, A. Ferraris and M. Carello, «Modeling and experimental validation of vehicle’s electric powertrain», in *2022 IEEE International Conference on Environment and Electrical Engineering and 2022 IEEE Industrial and Commercial Power Systems Europe (EEEIC / I&CPS Europe)*, Prague, 2022, doi: 10.1109/EEEIC/ICPSEurope54979.2022.9854612.

- [60] I. Arsie, M. Battistoni, P. P. Brancaloni, R. Cipollone, E. Corti, D. Di Battista, F. Millo, A. Occhicone, B. Peiretti Paradisi, L. Rolando e J. Zembi, «A New Generation of Hydrogen-Fueled Hybrid Propulsion Systems for the Urban Mobility of the Future», *Energies*, vol. 17, n. 34, 2024, doi: 10.3390/en17010034.
- [61] M. Spano, A. Shiledar, S. Gupta, M. Villani, D. Misul, M. Canova e G. Rizzoni, «Performance Evaluation of an Eco-Driving Controller for Fuel Cell Electric Trucks in Real-World Driving Conditions», in *SAE World Congress Experience (WCX24)*, Detroit, 2024, doi: 10.4271/2024-01-2183.
- [62] A. Feyijimi, A. von Jouanne, B. Phillips, E. Agamloh e A. Yokochi, «High Performance Electric Vehicle Powertrain Modeling, Simulation and Validation», *Energies*, vol. 14, n. 5, 2021, doi: 10.3390/en14051493.
- [63] S. R. Deshpande, S. Gupta, A. Gupta e M. Canova, «Real-Time Ecodriving Control in Electrified Connected and Autonomous Vehicles Using Approximate Dynamic Programing», *Journal of Dynamic Systems, Measurements, and Control*, vol. 144, n. 1, 2022, doi: 10.1115/1.4053292.
- [64] M. Acquarone, F. Miretti, P. G. Anselma e D. A. Misul, «Online Temperature-Aware Equivalent Consumption Minimization Strategy for Mild Hybrid Electric Powertrains», *IEEE Transactions on Vehicular Technology*, vol. 73, n. 4, pp. 4646-4658, 2024, doi: 10.1109/TVT.2024.3355181.
- [65] T. Letrouvé, A. Bouscayrol, W. Lhomme, N. Dollinger e F. Mercier Calvairac, «Different models of a traction drive for an electric vehicle simulation», in *2010 IEEE Vehicle Power and Propulsion Conference*, Lille, 2010, doi: 10.1109/VPPC.2010.5729209.
- [66] J. Zhou, X. Shen e D. Liu, «Modeling and simulation for electric vehicle powertrain controls», in *2014 IEEE Conference and Expo Transportation Electrification Asia-Pacific (ITEC Asia-Pacific)*, Beijing, 2014, doi: 10.1109/ITEC-AP.2014.6940824.
- [67] D. W. Gao, C. Mi e A. Emadi, «Modeling and Simulation of Electric and Hybrid Vehicles», *Proceedings of the IEEE*, vol. 95, n. 4, pp. 729-745, 2007, doi: 10.1109/JPROC.2006.890127.
- [68] H. Yang, Y. Chen, W. Li, X. He, W. Sun, Y. Chi e Y. Li, «Average-value model of modular multilevel converters considering capacitor voltage», in *2016 IEEE Applied Power Electronics Conference and Exposition (APEC)*, Long Beach, 2016, doi: 10.1109/APEC.2016.7468061.
- [69] S. Pal, M. G. Majumder, R. Rakesh, R. K. Mahapatra, K. Gopakumar and L. Umanand, «A Nine Level Inverter Topology with Linear Operation at Over-modulation Region», in *2020 IEEE 29th International Symposium on Industrial Electronics (ISIE)*, Delft, 2020, doi: 10.1109/ISIE45063.2020.9152214.
- [70] B. K. Bose, *Modern Power Electronics and AC Drives*, 1 ed., Upper Saddle River, New Jersey: Prentice Hall, 2002, p. 689, isbn: 0130167436.
- [71] A. M. Trzynadlowski, *Control of induction motors*, 1 ed., Amsterdam: Elsevier Science Publishing Co Inc, 2000, p. 201, isbn: 9780080503080.
- [72] J.-P. Louis, *Control of Synchronous Motors*, 1 ed., Hoboken, New Jersey: John Wiley & Sons, 2011, p. 398, doi: 10.1002/9781118601785.
- [73] G. L. Plett, *Battery Management Systems, Volume I: Battery Modeling*, 1 ed., Boston, Massachusetts: Artech House, 2015, p. 336, doi: isbn: 978-1630810238.
- [74] G. L. Plett, *Battery Management Systems, Volume II: Equivalent-Circuit Methods*, vol. 1, Boston, Massachusetts: Artech House, 2015, p. 336, isbn: 978-1630810276.
- [75] J. Larminie and A. Dicks, *Fuel Cell Systems Explained*, Hoboken, New Jersey: John Wiley & Sons, 2003, doi: 10.1002/9781118878330.
- [76] T. Lažek, I. Pazdera and M. Toman, «Comparison and Simulation of Two Loss Minimization Algorithms for Field-oriented Control of Induction Motor», in *2022 IEEE 20th International Power Electronics and Motion Control Conference (PEMC)*, Brasov, 2022, doi: 10.1109/PEMC51159.2022.9962920.
- [77] M. Toman, R. Cipin, P. Vorel and M. Mach, «Algorithm for IM Optimal Flux Determination Respecting Nonlinearities and Thermal Influences», in *2018 IEEE International Conference on Environment and Electrical Engineering and 2018 IEEE Industrial and Commercial Power Systems Europe (EEEIC / I&CPS Europe)*, Palermo, 2018, doi: 10.1109/EEEIC.2018.8493953.
- [78] M. Toman, R. Cipin, M. Mach and P. Vorel, «Application of acceleration method for evaluation of induction motor torque-speed characteristics», in *2017 IEEE International Conference on Environment and Electrical Engineering and 2017 IEEE Industrial and Commercial Power Systems Europe (EEEIC / I&CPS Europe)*, Milan, 2017, doi: 10.1109/EEEIC.2017.7977585.
- [79] J. Pyrhonen, T. Jokinen and V. Hrabovcova, *Design of Rotating Electrical Machines*, 1 ed., John Wiley, 2009, p. 538, isbn: 9780470695166.
- [80] The MathWorks, Inc, «MathWorks Help Center,» [Online]. Available: <https://it.mathworks.com/help/vdynblks/ref/longitudinaldriver.html>. [Accessed 14 07 2023].
- [81] Á. Fehér, S. Aradi and T. Bécsi, «Hierarchical Evasive Path Planning Using Reinforcement Learning and Model Predictive Control», *IEEE Access*, vol. 8, pp. 187470-187482, 2020, doi: 10.1109/ACCESS.2020.3031037.
- [82] «BS ISO 3888-2:2011; Passenger Cars—Test Track for a Severe Lane-Change Manoeuvre, ISO International Standards,» 2011. [Online]. Available: <https://www.iso.org/standard/57253.html>.

- [83] EMRAX d.o.o., [Online]. Available: https://emrax.com/wp-content/uploads/2020/03/emrax_268_technical_data_table_graphs_5.4.pdf. [Accessed 10 September 2022].
- [84] L. Ydrefors, M. Hjort, S. J. J. Kharrazi and A. Stensson, «Rolling resistance and its relation to operating conditions: A literature review», *Proceedings of the Institution of Mechanical Engineers, Part D: Journal of Automobile Engineering*, vol. 235, n. 12, pp. 2931-2948, 2021, doi: 10.1177/09544070211011089.
- [85] M. Guiggiani, *Dinamica del veicolo*, 1, Torino: CittàStudi, 2007, p. 384, isbn: 978-88-251-7300-0.
- [86] G. Genta, *Meccanica dell'autoveicolo*, 1, Torino: Levrotto & Bella, 2000, p. 568, isbn: 978-8882180423.
- [87] R. W. De Doncker, D. W. Pulle and A. Veltman, *Advanced Electrical Drives*, 2, Cham: Springer, 2020, p. 419, doi: 10.1007/978-3-030-48977-9.
- [88] D. Cittanti, A. Ferraris, A. Airale, S. Fiorot, S. Scavuzzo and M. Carello, "Modeling Li-Ion Batteries for Automotive Application: a Trade-Off between Accuracy and Complexity", in *International Conference of Electrical and Electronic Technologies for Automotive*, Turin, 2017, doi: 10.23919/EETA.2017.7993213.
- [89] United Nations Economic Commission for Europe, "UN Regulation No. 154 - Worldwide harmonized Light vehicles Test Procedure (WLTP)," [Online]. Available: <https://unece.org/transport/documents/2021/02/standards/un-regulation-no-154-worldwide-harmonized-light-vehicles-test>. [Accessed 17 01 2024].